The Spatiotemporal Structure of 20th Century Climate Variations in Observations and Reanalyses. Part I: Long-term Trend

Junye Chen[1,2], Anthony D. Del Genio[3], Barbara E. Carlson[3], Michael G. Bosilovich[2]

[1]Earth System Science Interdisciplinary Center
University of Maryland, College Park
College Park, Maryland

[2]Global Modeling and Assimilation Office
NASA Goddard Space Flight Center
Greenbelt, Maryland

[3]NASA Goddard Institute for Space Studies
New York, New York

Submitted to Journal of Climate
April 19, 2007

Revised, October 10, 2007

Corresponding author:
Junye Chen
NASA/GSFC Code 610.1
Greenbelt, MD 20771-0001
Phone: 301-614-6173
Email: jchen@gmao.gsfc.nasa.gov

ABSTRACT

The dominant interannual El Niño–Southern Oscillation phenomenon (ENSO) and the short length of climate observation records make it difficult to study long-term climate variations in the spatiotemporal domain. Based on the fact that the ENSO signal spreads to remote regions and induces delayed climate variation through atmospheric teleconnections, we develop an ENSO-removal method through which the ENSO signal can be approximately removed at the grid box level from the spatiotemporal field of a climate parameter. After this signal is removed, long-term climate variations are isolated at middle and low latitudes in the climate parameter fields from observed and reanalysis datasets. This paper addresses the long-term global warming trend (GW); a companion paper concentrates on Pacific pan-decadal variability (PDV).

The warming that occurs in the Pacific basin (approximately 0.4K in the 20th century) is much weaker than in surrounding regions and the other two ocean basins (approximately 0.8K). The modest warming in the Pacific basin is likely due to its dynamic nature on the interannual and decadal time scales and/or the leakage of upper ocean water through the Indonesian Throughflow.

Based on the NCEP/NCAR and ERA-40 reanalyses, a comprehensive atmospheric structure associated with the GW trend is given. Significant discrepancies exist between the two datasets, especially in the tightly coupled dynamics and water vapor fields. The dynamics fields based on NCEP/NCAR, which show a change in the Walker Circulation, are consistent with the GW change in the surface temperature field. However, intensification in the Hadley Circulation is associated with GW trend in ERA-40 instead.

1. Introduction

The global warming (GW) trend in the past hundred years or so has been a concern and debated by climate scientists since the late 1930s (Callendar 1938) or even earlier ages (Weart 2003). In recent decades, based on carefully calibrated global surface temperature (ST) records, a consensus has been gradually reached that the global mean temperature increased by about 0.8K during the 20th century (Ellsaesser et al. 1986; Hansen and Lebedeff 1987; Jones et al. 1999; Hansen et al. 1999; and other references therein), which is unprecedented in the most recent millennium of the Earth's history (Mann et al. 1999). These studies indicate a relatively uniform warming over the earth's surface, except that the warming over land and higher latitudes is stronger than over ocean and lower latitudes. The spatial distribution of the trends is roughly consistent with general circulation model simulations forced by anthropogenic greenhouse gas and aerosol increases.

Schneider and Held (2001) use discriminant analysis to decompose the long-term ST field. The GW trend appears to be the first discriminant in their analysis. Based on its spatial pattern, they suggest that this trend results from an increase in anthropogenic radiative forcing. Because they acquire the long-term trend discriminant by maximizing the ratio of interdecadal variance to intradecadal variance, it is difficult to use this method to detect long-term climate change in other datasets with shorter time periods.

Accompanying the global surface warming trend, there must be systematic changes in the atmospheric structure, circulation and hydrologic cycle. Global atmospheric profile data come from radiosonde network and satellite sounding data in more recent decades. Temperature trends derived from these data have disagreed with each other and with

global climate model predictions, but the derived trends have begun to converge as understanding of discontinuities and biases in sonde records and satellite data has increased (Karl et al. 2006). Suffering little from spatial and temporal subsampling, reanalysis products that assimilate observations into a global weather prediction model (Kalnay et al. 1996; Kistler et al. 2001; Uppala et al. 2005) can potentially be used to diagnose aspects of long-term changes in the atmosphere (Santer et al. 2004; Trenberth and Smith 2005; Trenberth et al. 2005; Mitas and Clement 2005; Mitas and Clement 2006).

Although the reanalyses are produced with a fixed model and analysis system, the input observations are not homogeneous due to historical changes in the observing system, especially when new kinds of observations are introduced. After 1948, the beginning of the longest NCEP/NCAR reanalysis, two major changes occurred in the global observing system: the global radiosonde network was established in 1958, and the global operational satellite observation system was introduced in the 1970s.

Several studies have indicated limitations of the reanalysis products for global climate change studies. Kistler et al. (2001) show that the strongest impact of the introduction of satellite observations in 1979 on the NCEP/NCAR reanalysis is above 200hPa and south of 60°S. The discontinuities in the lower stratosphere and upper troposphere around 1979 are caused by biases from both the NCEP model and NESDIS retrievals (Santer et al. 1999). Sturaro (2003) finds that the spurious shifts in the temperature fields in 1979 are broader than earlier estimates: though the biggest changes still occurred around the 100hPa level, the affected regions include the tropics between 700 and 50hPa and the southern ocean region between 500 and 250hPa. For the ERA-40 reanalysis, Bengtsson et

al. (2004a) argue that the changes in the observing system have had huge impacts on the global mean linear trends of temperature, integrated water vapor, and kinetic energy.

The time periods covered by reanalysis datasets are on the order of decades, which is too short to derive reliable regional GW trends. For example, the linear trend in equatorial Eastern Pacific sea surface temperature (SST) is strongly positive during the second half of the 20th Century, because of the 1976 climate regime shift in the Pacific basin, but it is very weak over the entire century. The 1976 shift is one of several offsetting phase changes associated with natural pan-decadal variability (PDV) in the Pacific basin over the past century (see Zhang et al. 1997, among others).

Another complicating factor is the dominant interannual El Niño–Southern Oscillation (ENSO) phenomenon. When a dataset is long enough, a low pass filter can be applied to remove the ENSO signal before attempting to isolate other modes of variability using techniques such as empirical orthogonal function (EOF) analysis (Zhang et al. 1997). But if the record is too short to apply a low pass filter, then ENSO not only dominates the first EOF but also contaminates several following modes, as shown in Appendix A. The reason is that the ENSO signal appears in remote regions away from the tropical Pacific with a time delay of a few months due to atmospheric teleconnections or ocean dynamics. The contamination of the following modes prevents the isolation of other aspects of climate variability.

To extract long-term climate information from limited and imperfect data, we describe in this paper an ENSO-removal method that is based on the observation that regional ENSO effects can be approximately described by a lead/lag relationship between the Niño-3.4 ENSO index and the local anomaly time series (Trenberth et al. 2002). After

ENSO is removed, the GW trend and PDV are isolated as the leading modes in EOF analyses of ST datasets; however, the results are unstable, if based on individual parameters from the reanalyses. The reason is unclear but appears to be related to the unevenly distributed discontinuities in the reanalyses.

A systematic investigation is therefore performed on the discontinuity issue in the NCEP/NCAR and ERA-40 reanalyses (Appendix B). Temporal discontinuities in the reanalyses are not uniformly present in different parameters or coherently distributed in different regions and pressure levels. On the other hand, the real climate signal should be distributed across multiple parameters in a more coherent fashion. Thus, the effects of artificial discontinuities can be reduced if a large number of parameter fields are included in a combined EOF analysis. We perform such an analysis for both reanalyses, in an attempt to isolate the GW trend and PDV signals in atmospheric thermodynamic structure and circulation fields. This paper concentrates on the GW trend, while a companion paper (Chen et al. 2007a, hereafter referred to as Part II) focuses on the PDV mode.

2. Data and analysis procedures

a. Datasets

1.) Surface temperature

In this study, two long-term monthly global ST datasets are used. The first is a SST dataset, the extended reconstruction of global SST version 2 (ERSST.V2) (Smith and Reynolds 2003; Smith and Reynolds 2004), which is based on SST data in the International Comprehensive Ocean-Atmosphere Dataset (ICOADS) (Slutz et al. 1985, Worley et al. 2005) from 1854 to the present. ICOADS is a global dataset based on in situ

marine observations. ERSST.V2 is an improved version of ICOADS SST with updated quality control procedures and advanced reconstruction methods. The data are reliable after 1880, and the uncertainty decreases to a minimum after 1950. The other ST dataset is the NASA GISS surface temperature (GISTEMP) analysis (Hansen et al. 1999), which is a combination of land surface air temperature (SAT) observed by meteorological stations and SST observed by ships. In GISTEMP, land SAT is based on the Global Historical Climatology Network dataset, and SST is based on the Met Office Hadley Centre's sea ice and SST dataset (HadISST1) (Rayner et al. 2003) from 1880 to November 1981 and the NOAA Optimum Interpolation SST V2 dataset (NOAA OI SST V2) (Reynolds et al. 2002) from December 1981 to present. ERSST.V2 is the latest version of the SST dataset available; thus, we use it in the calculation of the ENSO index and in an ocean-only analysis. For a global analysis covering both land and ocean, we use GISTEMP instead.

2.) Atmospheric parameter fields from reanalyses

In addition to the two ST datasets, 5 atmospheric parameters at 8 pressure levels (1000hPa, 925hPa, 850hPa, 700hPa, 600hPa, 500hPa, 400hPa, 300hPa) from the NCEP/NCAR and ERA-40 reanalyses are analyzed. These parameters—air temperature (T_{air}), zonal wind speed (U), meridional wind speed (V), vertical velocity (ω), and specific humidity (q) —are in the higher reliability classes of the NCEP/NCAR reanalysis products. T_{air}, U, and V are ranked in Class A, and ω and q are ranked in Class B, indicating that these parameters depend more on observations than on the NCEP model especially so for A parameters (Kalnay et al. 1996). The same should be true for ERA-40

(Uppala et al. 2005), which assimilates similar and additional radiosonde and satellite sounding data, though no ranking system is provided.

b. Data processing and analysis procedures

For each parameter at each grid point, the long-term mean annual cycle was subtracted from the original monthly time series to obtain the anomaly time series. The long-term mean annual cycle for the STs is based on the period 1982 to 2000, following the definition of GISTEMP. For the reanalyses, we use 1968 to 1996, consistent with that used by the NCEP/NCAR reanalysis. The difference in the definition of annual cycle has negligible effects on the analysis results.

Next, the ENSO-removal method (see Appendix A) was applied to the anomaly time series of each parameter at each grid point. Then, the ENSO-removed ST data were analyzed using EOF analysis for 60S-60N from 1900 to 2003. The GISTEMP and ERSST.V2 analyses were performed based on the covariance matrix of the parameter field, and the components of the matrix were weighted by the area of the corresponding grid. Before EOF analysis, in order to emphasize the long-term variations, the ENSO-removed monthly time series at each grid is smoothed with an annual average filter (with weights: 1., 1.5, 3., 4.5, 5.5, 6.5, 7., 6.5, 5.5, 4.5, 3., 1.5, 1.) and then adjusted to a zero mean by subtracting its mean value from each point of the time series.

The ENSO-removed reanalysis monthly atmospheric parameter fields were interpolated to 5° x 5° resolution, then were smoothed with the annual average filter and adjusted to a zero mean at each grid point. Each parameter field was normalized by dividing the standard deviation of the whole spatiotemporal field of this parameter, thus providing similar weights. Then, the rescaled parameter spatial fields at each month were

put together to construct a combined field, which includes the normalized spatial patterns of the 40 parameters. After the EOF analysis was applied to the time series of the combined field, the resulting EOF of each mode was separated back into 40 individual spatial patterns, one for each parameter. The 40 patterns share the PC time series; that is, a given mode depicts related variations in all the parameters. As in the ST EOF analyses, the spatial domain of the combined EOF analyses is also over the 60°S-60°N zonal band. The time period is from 1970 to 2003 (NCEP/NCAR) and from 1970 to 2002 (ERA-40). The starting point of 1970 was chosen for the combined EOF analyses to include the 1976 climate regime shift and to exclude the relatively low quality reanalysis data before the 1970s (as shown in Appendix B). The combined EOF analyses based on reanalysis datasets are abbreviated as the NCEP1-40p and ERA40-40p analyses, respectively.

3. The global warming trend mode in the ST field

The mean anomaly ST time series (Figure 1, black line) based on GISTEMP data shows no obvious trend from 1900 to 1910. There was an increase (about 0.3K) in global ST from the mid- to late 1910s through the early 1940s, a slight cooling from the 1940s to the 1970s, and then the global ST increased again by about 0.5K from the 1970s through the late 1990s. The ENSO related deviation (Figure 1, dashed blue line), defined as the global mean ENSO signal based on the ENSO removal method in Appendix A, is mostly around ±0.1K, with only a few exceptional El Niño events reaching the level of 0.2K. The ENSO-removed ST time series retains most of the long-term variability in the original ST time series.

We can also see from Figure 1 that the principal component (PC) (Figure 1, red line,

which is scaled to represent the global mean ST change associated with the EOF mode) of the first mode (27.3% variance explained) of the GISTEMP analysis matches well the original global average ST time series, in both its low frequency characteristics and the magnitude of the long-term increase. This mode will hereafter be called the global warming (GW) trend mode. The GW trend mode also appears to be the dominant mode of the ERSST.V2 analysis (Figure 1, green line). Both PC time series share the same long-term trend with few differences and are consistent with the global average temperature trend.

The EOF spatial patterns of the GW mode (Figure 2) show that most of the earth's surface warmed in the 20th century. The GW spatial patterns suggest a response to globally imposed radiative forcing rather than a long-term internal oscillation of the ocean circulation, which usually appears as a polarized structure in the SST field (Schneider and Held 2001). The locations of the cooling regions over land approximately coincide with the regions with negative radiative forcing from sulphate aerosol, organic aerosol, soil dust, and land-use change (Hansen et al. 1998; Haywood et al. 1997; Penner et al. 1998; Tegen et al. 1996). The connection between aerosol loading and the regional cooling trend over land has been noted in previous studies (Hansen et al. 1998; Karl et al. 1995; Mitchell and Johns 1997). Generally, warming over land is substantially stronger than over the ocean due to the large thermal inertia of the ocean compared to the negligible heat storage capability of the land and the smaller evaporative cooling over dry land (Trenberth et al. 2007). The warming over high latitudes is stronger than over low latitudes because of the positive temperature-albedo feedback caused by snowcover and the absence of convective heat removal at high latitudes.

The ocean-only spatial pattern of the ERSST.V2 trend mode (Figure 2, lower) is not identical to the ocean part of the GISTEMP trend mode pattern (Figure 2, upper) (correlation coefficient: 0.43). An ocean-only analysis applied to GISTEMP (not shown) has a nearly identical trend mode to that from the original GISTEMP analysis: the correlation coefficients are 0.97 and 0.99 for the PC time series and the EOF spatial pattern, respectively. Thus, the difference in spatial patterns stems from the disagreement between the two datasets, which are different in historical bias corrections, input data and analysis procedures (Smith and Reynolds 2003; Smith and Reynolds 2004; Rayner et al. 2003). There is almost no cooling in the Pacific anywhere in ERSST.V2. The warming along the west coast of South America and over the Central Pacific region is stronger in ERSST.V2, while warming off the west coast of North America is larger in GISTEMP. Furthermore, there are differences in the detailed features of the two patterns over the Indian and Atlantic Oceans. Otherwise, the patterns from GISTEMP and ERSST.V2 are generally consistent in their global scale ocean warming patterns.

The average warming over the Pacific is much weaker than over the Atlantic and Indian Oceans in both datasets. This feature has not been emphasized by previous observational studies, though it can be seen in local ST linear trend maps, for example in Figure 3.9 of the IPCC Fourth Assessment Report (AR4) (Trenberth et al. 2007), in which it was attributed to Pacific Decadal Oscillation effects. There is no sign of this feature in the multi-model ensemble annual mean ST change based on different scenarios in Figure 9.6 of the AR4 report (Hegerl et al. 2007). The weakened warming in the Pacific basin is consistent with the ocean heat content change in the analysis of Levitus et al. (2000). About half of the increased heat is stored in the upper 300 meters of the

Atlantic and Indian Oceans. In the Pacific Ocean, however, the heat content in the upper 300 meters seems to have stronger decadal variability and a small increasing trend, which is consistent with our weaker Pacific SST increase.

It is natural to ask why the warming in the Pacific Ocean is weaker than in other ocean basins. First, the largest interannual and decadal variability in middle and low latitude ocean dynamics, due to ENSO and PDV, is located in the Pacific basin. ENSO involves large heat storage and release on interannual time scales (Trenberth et al. 2002). The same is probably also true for the decadal oscillation in the Pacific. Thus, radiative heating anomalies may mix more easily to the deeper ocean and/or be released to the atmosphere, instead of being stored in the upper ocean, thus diminishing surface warming in the Pacific basin.

Another possible influence on the Pacific is the Indonesian Throughflow (ITF). Warming induced by radiative forcing is concentrated in the upper levels of the ocean. In the Pacific, surface mixed layer and thermocline water are continuously exported to the Indian Ocean through the ITF; the lost upper level water is replaced by cold lower level water from the southern ocean. Through this renewal process, at least part of the heat from radiative forcing is transported from the Pacific Ocean to the Indian Ocean. The amplitude of this cooling effect can be roughly estimated through the following assumptions: i.) the temperature increase occurs uniformly in the upper 300 meters; ii.) the temperature increase rate in the Pacific Ocean would equal the global mean ST increase rate if there were no leakage through the ITF; iii.) the ITF transport is 5 Sv in the upper 300 meters (about half of the total ITF transport that occurs down to 700 m, 1 Sv = $10^6 m^3 s^{-1}$) (Song et al. 2004; Susanto and Gordon 2005); iv.) the ITF water is only from

the upper 300 meters of the Pacific Ocean; and v.) the temperature of the southern ocean water that replaces the ITF water is stable. The change in temperature in the upper 300 meters of the Pacific Ocean can be expressed as:

$$dT(t) = R \cdot dt - ITF \cdot \frac{T(t) - T(0)}{V} \cdot dt \qquad (1)$$

where T denotes temperature; t refers to time (t=0 is assumed here to be 1900); R is the global mean ST increase rate (0.8K per century); ITF is the ITF flux (approximately 5 Sv, treated as constant); and V is the volume of the water mass in the upper 300 meters (5.43×10^{16} m^3) of the Pacific. The solution of (1) is

$$\Delta T = \frac{R \cdot V}{ITF} \cdot (1 - e^{-\frac{ITF}{V}\Delta t}) \qquad (2)$$

Thus, in the last century (Δt = 100 years), the temperature change in the Pacific Ocean estimated from (2) is $\Delta T \sim$ 0.7K. The difference between the global mean temperature increase and ΔT is 0.8K - 0.7K = 0.1K. This implies a 0.15K difference between the Pacific and the rest of world. ITF could be a factor in the weakened warming of the Pacific Ocean.

The warming pattern in the Indian Ocean is also modified by the ITF. Although the average warming in the Indian Ocean is much stronger than in the Pacific Ocean, the relatively weaker warming east of Madagascar (Figure 2) may be caused by the upwelling of the relatively cooler ITF water that is transported from the Indonesian Sea to the West Indian Ocean in the thermocline (Song et al. 2004). Along the west coast of the Indian Ocean, the Agulhas Current transports warm water from low latitudes to southern middle latitudes. The strong warming in the South Indian Ocean (around 40°S) probably is caused by the retroflection of the Agulhas Current (Gordon 2001) near the south end of

Africa. Part of the Agulhas water enters the South Atlantic, thus contributing to the strong warming in the Southeast Atlantic region.

The northern North Atlantic Ocean appears to be weakly cooling (Figure 2). This feature has been simulated and attributed to a reduction of poleward heat transport resulting from the weakening of thermohaline circulation, initiated by an increase in the freshwater input at high latitudes (Cubasch et al. 2001). Another possible reason is the strong positive phase of the North Atlantic Oscillation in the 1980s and 1990s (Scaife et al. 2005), which causes southward Ekman drift of cold polar water and advection of cold air from Labrador.

4. The GW trend mode manifested in the atmospheric fields of reanalyses

Figure 3 shows the dominant mode PCs from both the NCEP1-40p (red line) and ERA40-40p (black line) analyses and the 1970 to 2003 segment of the GW trend mode PCs of the GISTEMP (dotted blue line) and ERSST.V2 (dotted green line) analyses. The NCEP1-40p and ERA40-40p PCs share a similar long-term increasing trend with the GISTEMP and ERSST.V2 PCs though they are not identical. During the early 1970s, the NCEP1-40p and ERA40-40p PCs are more negative than the GISTEMP and ERSST.V2 PCs. This difference is unlikely to be caused by the satellite discontinuity effect on the reanalysis data, as all the curves agree after 1975. The timing may instead suggest gaps in sampling of the 1976 climate shift by the radionsonde network. The early 1990s minimum in the GISTEMP PC, due to the 1991 Mount Pinatubo eruption, is not so obvious in the ERSST.V2 PC and NCEP1-40p PC and is absent in the ERA40-40p PC. This difference is plausible for NCEP1-40p and ERA40-40p, because volcanic aerosol

forcing is not explicitly included in the reanalyses. In the ocean-only GISTEMP analysis (not shown), the volcanic signal is weaker than in the original GISTEMP analysis but still larger than in ERSST.V2. Therefore, the diminished volcano signal in the ERSST.V2 analysis is caused not only by the resistance of the ocean to the transient volcano aerosol forcing but also by the difference between the two datasets. Otherwise, the NCEP1-40p and ERA40-40p PCs match the GISTEMP PC and the ERSST.V2 PC well, considering that they are based on different parameter fields and time ranges.

The spatial patterns of the atmospheric temperature changes associated with the trend mode are shown in Figure 4 (NCEP1-40p in left column; ERA40-40p in right column). Warming is prevalent at all tropospheric levels for both NCEP1-40p and ERA40-40p. This is consistent with global radiative forcing, and with the increase of tropospheric temperature projected by climate models forced by natural and anthropogenic radiative forcings (Hansen et al. 2002, Karl et al. 2006).

The near surface T_{air} patterns from the NCEP1-40p (Figure 4, left bottom) and ERA40-40p (Figure 4, right bottom) analyses differ in some ways from the ST pattern from the 1900 to 2003 GISTEMP and ERSST.V2 analyses, especially outside the tropics (Figure 2). This discrepancy mainly results from the different time ranges. The correlation coefficient between the NCEP1-40p 1000hPa pattern (Figure 4-12 in Chen 2005) and the GISTEMP pattern becomes much greater (rising from 0.46 to 0.71) when the GISTEMP 1900–2003 spatial pattern (Figure 2, upper) is replaced by the GISTEMP 1970–2003 spatial pattern (Figure 4-13 in Chen 2005).

In NCEP1-40p, the temperature increase at the 850hPa level is larger than at the levels below (925hPa) and above (700hPa), over the South Indian Ocean and Southeast

Pacific regions (Figure 4 left column, but shown more clearly in Figure 4-12 of Chen 2005). In the middle troposphere of ERA40-40p and the upper troposphere of NCEP1-40p, warming in the southern middle latitudes is suspiciously high. The temperature discontinuity patterns of NCEP/NCAR and ERA-40 (Appendix B, Figure B2) suggest that these might be artifacts of satellite discontinuity in the 1970s.

Although T_{air} patterns (Figure 4) are contaminated by the above artifacts, moderate to high correlations in T_{air} patterns between the two reanalyses (Table 1) imply useful information content, considering they are based on different models, input observations and assimilation systems. Broad warming patterns indicate similar trend directions with observations (Lanzante et al. 2006) and GCMs (Santer et al. 2006). At the same time, the contamination from discontinuities makes it hard to answer a more subtle question based on reanalyses: whether the troposphere has warmed more than the surface? The answer is positive based on GCM simulations (Santer et al. 2006), but still not in consensus in different observation datasets (Lanzante et al. 2006). The proposed new reanalyses (Folland et al. 2006), for example, Modern Era Retrospective-analysis for Research and Applications (MERRA, http://gmao.gsfc.nasa.gov/research/merra/), focusing more on hydrological cycle and climate homogeneity, will help to solve this problem.

In Figure 5, atmospheric dynamics changes at 850, 500 and 300hPa associated with the trend mode of NCEP1-40p (left column) and ERA40-40p (right column) are shown. In general, the dynamical fields significantly differ between the two reanalyses. For NCEP1-40p, a strong 850hPa divergence trend (Figure 5, bottom left) appears in the equatorial Central Pacific, while convergence trends exist in the Amazon, East Pacific, West Pacific, and equatorial Indian Ocean. In the middle troposphere (Figure 5, middle

left), these features appear as corresponding 500hPa descent/ascent trends, but on somewhat broader spatial scales. The ascending anomalies imply that convective activity over the Maritime Continent and Amazon basin should have increased in association with the GW trend. In the Central Pacific, the strong subsidence feature extends to the northern and southern Pacific at weaker intensity. Coherent with the middle troposphere vertical velocity field, the upper troposphere horizontal wind field (Figure 5, left top) diverges in the 500hPa ascending regions and converges in the descending region. The three-dimensional wind field defines an anomalous overturning circulation, which has one descending branch over the Central Pacific and two ascending branches over the western and eastern Pacific coastal regions. This anomalous overturning circulation is consistent with the large scale trend in the zonal SST gradient over the Pacific basin and its surrounding regions, caused by the weakened warming in the Pacific basin (Figure 2).

For ERA40-40p (Figure 5, bottom right), a chain of 850hPa convergence anomalies circles most of the earth roughly along the equator, and divergence appears over the subtropical Pacific. Consistent with this, middle troposphere ascending motion (negative ω) (Figure 5, right middle) dominates in the vicinity of the equator, except over Africa; descending motion is prevalent in the subtropics. In the upper troposphere (Figure 5, right top), strong divergence (convergence) appears more in the equatorial (subtropical) regions. This describes a coherent three-dimensional dynamic change in the GW mode of ERA40-40p: more convective activity occurs in the equatorial region and more subsidence motion in the subtropical regions, indicating an intensification of the Hadley circulation (Mitas and Clement 2005).

The long-term mean of the dynamical fields and the changes in these associated with the GW trend mode in the two reanalyses are summarized in the 10°S-10°N meridional mean zonal cross section and zonal mean meridional cross section wind fields shown in Figure 6. The two reanalysis datasets are similar in the climatological mean overturning circulations (Figure 6, green vectors). The zonal mean Hadley circulation (upper panels) has climatological ascending motion from 10°S-10°N, with a maximum at ~7.5°N; descending motion occurs at 15°-40° in both hemispheres. The climatological 10°S-10°N meridional mean Walker circulation (Figure 6, lower, green vectors) has a dominant convection center over the Maritime Continent and West Pacific warm pool (80°E-180°E) region, and two secondary ascending regions over the Amazon (around 60°W) and Central Africa (around 20°E). Consistent with the strong ascent, the upper level zonal wind diverges over the warm pool and flows toward the surrounding central-eastern Pacific and West Indian Ocean.

The overturning circulation changes associated with the GW trend mode significantly differ between NCEP1-40p and ERA40-40p, as expected from Figure 5. For NCEP1-40p, the Walker circulation change (Figure 6, lower left, black vectors) is an order of magnitude stronger than that in the Hadley cell (Figure 6, upper left, black vectors). For ERA40-40p, the intensification in the Hadley cell is much more systematic than changes in the Walker circulation. However, the ERA40-40p anomalous ascending maximum is located south of the equator, as opposed to north of the equator where the climatological maximum occurs.

As shown in Figure 7, the water vapor changes differ dramatically in the two reanalyses. In NCEP1-40p, consistent with the broad surface warming (Figure 2), q

broadly increases near the surface 1000hPa and 925hPa levels (the latter is not shown). In the middle to upper troposphere, the water vapor concentration seems tightly coupled with the dynamics (Trenberth et al. 2005). Strong drying in the middle troposphere (Figure 7, two middle left plots) over the Central Pacific is consistent with the strong descending branch of the anomalous zonal overturning circulation (Figure 5 middle left, Figure 6 lower left); at the same time, strong moistening (Figure 7, the 2 middle left plots) occurs in both the western and eastern Pacific ascending branches (Figure 5 middle left, Figure 6 lower left). In the upper troposphere, moistening is strong over the East Pacific and Amazon region, but drying now occurs over the Maritime Continent region. This asymmetric change might be attributed to the stronger anomalous ascending motion over the east equatorial Pacific and Amazon region (Figure 5 middle left, Figure 6 lower left), thus allowing more water vapor to be transported to the upper troposphere, in comparison with the situation over the Maritime Continent region.

In ERA40-40p, the water vapor change is closely associated with the anomalous intensification of the Hadley circulation in the middle to lower troposphere. Strong moistening happens in the ±20° band where the ascending branch of the Hadley circulation is located; drying appears in the subtropical and middle latitudes, where the descending branches of the Hadley circulation occur. From the 600hPa to the upper pressure levels, the tropical moistening feature weakens, and subtropical drying strengthens and expands into the tropics, except for the Indonesian and Amazon regions.

5. Conclusion and discussion

In this study, the GW trend in the 20th century emerged as the dominant mode in the

ENSO-removed EOF analyses based on ST datasets. The relatively uniform warming implies that the global long-term trend should be attributed to relatively evenly distributed radiative forcing. The amplification of that warming in the middle-high latitude land regions is consistent with previous linear trend analyses (Ellsaesser et al. 1986; Hansen and Lebedeff 1987; Jones et al. 1999; Hansen et al. 1999) and anthropogenic greenhouse gas model simulations (Hegerl et al. 2007). Several embedded cooling spots that may be related to negative radiative forcing from sulfate aerosol, organic aerosol, soil dust, and land-use change (Hansen et al. 1998; Karl et al. 1995; Mitchell and Johns 1997) are also detected in our analysis.

Beyond these previously documented aspects of the 20th century long-term trend, we reveal another important characteristic of the GW trend: warming in the Pacific basin is much weaker than the warming at the east and west boundaries of the Pacific Ocean and in the other ocean basins. The modest warming in the Pacific basin is consistent with the long-term ocean heat content change (Levitus et al. 2000). We hypothesize that the weakened warming originates from the more dynamic nature of the Pacific Ocean on interannual and interdecadal time scales and/or the leakage of the upper ocean water through the Indonesian Throughflow. The failure of climate models to simulate these phenomena could explain why the apparent weakened warming in the Pacific basin has not appeared in the multi-model ensemble annual mean ST change based on different scenarios (Hegerl et al. 2007).

Changes in the atmospheric parameter fields associated with the GW trend have also been isolated from the NCEP/NCAR and ERA-40 reanalyses. The broad warming in both reanalyses at different pressure levels of the troposphere is consistent with an evenly

distributed radiative forcing, and the increasing trend PC time series are generally consistent with the PC time series based on century time scale ST analyses.

GW-related dynamics and water vapor changes are coherent within each reanalysis, but significant discrepancies exist between the two reanalyses. The main atmospheric circulation change in NCEP1-40p is a modification in the Walker circulation over the Pacific basin and its surrounding regions, with anomalous ascending moist branches over the Maritime Continent and East Pacific-Amazon regions and a descending dry branch over the Central Pacific. This anomalous zonal overturning circulation is consistent with the large scale zonal ST contrast caused by the weakened surface warming in the Pacific basin and the strong warming in surrounding regions. On the other hand, an anomalous intensification of the Hadley circulation appears to be the major dynamical feature of the GW trend mode in the ERA40-40p analysis, corresponding to strong moistening in the tropics and drying in the subtropics.

Besides the difference in the underlying models, which is not expected to have a large effect on long-term trends (Cai and Kalnay, 2005), significant differences exist between NCEP/NCAR and ERA-40 in what satellite data are assimilated and how, and these probably cause the discrepancies in dynamics and water vapor fields. In the NCEP/NCAR reanalysis, only retrieved atmospheric temperature profiles are assimilated. In the ERA-40 reanalysis, the radiances from satellite infrared channels are directly assimilated, including both temperature sensitive and water vapor sensitive channels. After 1987, the column integrated precipitable water retrieved from SSM/I microwave channels is also assimilated in ERA-40. That is, more water vapor data are included in the ERA-40 reanalysis than in the NCEP/NCAR reanalysis, where the major water vapor

data input is from radiosonde observations. Because the satellite data from different spacecraft are introduced at different times, the ERA-40 reanalysis has a more severe discontinuity issue in humidity fields than the NCEP/NCAR reanalysis (Appendix B, Figures B1 and B2). At the same time, the water vapor increment from the satellite data can artificially change the large scale circulation when additional latent heat is released through precipitation (Bengtsson et al. 2004b).

The signal/noise ratio of long-term climate variations can be enhanced (Santer et al. 2001) by removing the known signals of short-term climate phenomena, especially ENSO. Compared to the previous ENSO isolation attempts discussed in Appendix A, our ENSO isolation method keeps the simplicity of linear regression, yet considers the lag relationship between the N34h index and local time series. More sophisticated methods may be developed to address the nonlinear and asymmetrical aspects of ENSO. The GW trend time series obtained in this study is close to the trend time series in Kelly and Jones (1996). Although the trend time series in Penland and Matrosova (2006) is significantly different. The cause of this discrepancy is not clear, yet we notice that their ENSO signal includes long-term variation in the interdecadal time scale, traditionally not attributed to ENSO.

Combining multiple parameters in the EOF analysis helps to isolate the real climate signal in imperfect datasets, when the artifacts are not systematically distributed among parameters and across different regions. Aspects of the surface and atmospheric trend patterns that are common to both reanalyses and not associated with data discontinuities can be compared with model simulation results to confirm whether the GW trend is caused by anthropogenic forcing or natural variability, and/or to test and improve the

model capability to simulate climate change on regional scales. However, this study is based on annually smoothed anomaly data; thus, no seasonal information is included in the results. It is possible that long-term climate changes confined to specific seasons are not detected by our approach.

The weakened warming in the Pacific basin appears to be an important and consistent feature of the GW trend. We propose two possible mechanisms to explain this weakened warming in the Pacific basin. These hypotheses must be explored using model simulations emphasizing the long-term heat budget of the ocean and including realistic basin topography and proper simulation of the interannual and decadal variability. At the same time, other mechanisms may exist, for example, century time scale random variabilities, which could be verified based on the output of ensemble runs of the coupled models with the capability to realistically simulate long-term climate variations. Until this weakened warming in the Pacific basin is understood and incorporated in coupled model simulations, predictions of 21st Century regional climate changes in surrounding continental regions should be viewed circumspectly.

Acknowledgements: This research was supported by the NASA Climate Modeling and Analysis Program. We thank to Arnold Gordon, Mike Wallace, Mingfang Ting, Amy Clement and two anonymous reviewers for insightful suggestions. GISTEMP data were provided by Reto Ruedy at GISS, and can be downloaded at http://www.giss.nasa.gov/data/update/gistemp/. NOAA Extended Reconstructed SST data version 2 (ERSST.V2) were provided by the NOAA-CIRES Climate Diagnostics Center, Boulder, Colorado, USA, from their Web site at http://www.cdc.noaa.gov/. NCEP/NCAR reanalysis data were downloaded from http://www.cdc.noaa.gov/cdc/reanalysis/. The ERA-40 reanalysis monthly mean pressure level analysis data were downloaded from the European Centre for Medium-Range Weather Forecasts (ECMWF) website, http://www.ecmwf.int/products/data/archive/descriptions/e4/index.html

Appendix A ENSO Removal

a. Introduction

There have been several attempts to remove ENSO from the ST field (Kelly and Jones 1996). Jones (1988) regresses the high-pass filtered hemispheric- and global-mean ST time series on the Southern Oscillation Index (SOI) with SOI leading by six months, and then removes the regression result from the ST time series. Privalsky and Jensen (1995) use a bivariate autoregressive (AR) model to regress the global average air temperature on SOI. They find that more variance (about 30%) can be attributed to ENSO with the bivariate AR model than with a linear regression method (about 10%), which implies that ENSO affects surface air temperature with different time lags in different regions; thus, the global average temperature has a multi-lag relationship with SOI. Robock and Mao (1995) linearly regress the ST to SOI with no lag over the ocean and one season lag over land. They note that spurious small-scale patterns can be induced if a specific lag is applied to every grid box. Kelly and Jones (1996) identify the first and third modes in an EOF analysis of global ST as related to ENSO. They remove the ENSO signal based on the cross-correlations between the SOI and the principal component of these two EOF modes. Santer et al. (2001) remove ENSO and volcanic signals in the global mean surface and lower tropospheric temperature using an iterative procedure to account for the collinear relation between the ENSO and volcanic signals; they find more significant trends and better agreement between the observations and model simulations when the effects of ENSO are removed. Penland and Matrosova (2006) use linear inverse model to isolate the ENSO signal in a broad spectral range from interannual to interdecadal.

Recent advances in understanding of the mechanisms of ENSO and its remote effects (Neelin et al. 1998; Trenberth et al. 1998; Wallace et al. 1998; Harrison and Larkin 1998; Klein et al. 1999; Trenberth et al. 2002; Alexander et al. 2002; Carleton 2003) lead us to suggest a more reliable ENSO removal method at the grid box level, which we describe below.

b. The ENSO index and how ENSO affects remote regions

The primary surface manifestation of ENSO is a seesaw between West and East Pacific; thus, its phase and strength can be approximately depicted with an index. Hanley et al. (2003) comprehensively evaluate various indices and find strong similarities in the Niño-3, Niño-3.4, and JMA indices. Trenberth et al. (2002) suggest that Niño-3.4 is useful for systematically exploring lead and lag relationships in the evolution of ENSO. We therefore calculate the time series of the Niño-3.4 index, defined as the averaged SST anomaly in the eastern equatorial Pacific region of 5°N-5°S and 170°W-120°W, based on the SST field from ERSST.V2. Because ENSO is an interannual phenomenon, we remove the low frequency (decadal and longer) variability (Figure A1, green) with a six-year low pass filter (Zhang et al. 1997) from the original Niño-3.4 index time series (Figure A1, black). Hereafter, we will use the resulting six-year high-pass Niño-3.4 index (referred to as N34h) (Figure A1, red) to represent ENSO temporal variability.

Previous studies (Bjerknes 1969; Opsteegh and Van den Dool 1980; Hoskins and Karoly 1981; Webster 1981; Horel and Wallace 1981; Lau 1997; Trenberth et al. 1998; Wallace et al. 1998) address the fact that the tropical Pacific ENSO signal spreads to remote regions around the world through atmospheric teleconnection mechanisms. In the

zonal direction, the anomalous deep convective activities in the Central Pacific depress the regional circulation over the tropical Atlantic and Indian oceans, resulting in anomalous heating and delayed ST change (Lanzante 1996; Enfield and Mestas-Nunez 1999; Klein et al. 1999; Alexander et al. 2002; Chiang and Sobel 2002). In the meridional direction, associated with enhanced upper troposphere divergence in the central-eastern Pacific, strong upper troposphere convergence in the subtropics acts as a source of Rossby waves and thus induces teleconnection patterns, namely, the north-eastward Pacific-North America (PNA) pattern and south-eastward Pacific-South America (PSA) pattern (Carleton 2003). In these mechanisms, the atmosphere acts as a bridge to link the tropical Pacific to remote regions (Lau and Nath 1996, Klein et al. 1999). Associated water vapor (Klein et al. 1999), cloud (Fu et al. 1996), and wind (Enfield and Mayer 1997) variations affect the surface energy flux, adjusting the ST in remote regions over a few months. In the Pacific, ENSO-generated coastally trapped ocean waves (mainly Kelvin waves) propagate SST anomalies to high latitudes (Alexander et al. 2002).

From the upper plot of Figure A2, we see that ST is in phase with the N34h index in the central-eastern tropical Pacific, where the strongest extreme cross-correlations with the least lag (ECLL) appear (Figure A2, lower). In much of the extratropical Pacific and North America, ST lags N34h by 1 - 6 months and appears in patterns that alternate positive and negative ECLL with N34h and deflect eastward from low latitude to high latitude (Figure A2, lower). These features are consistent with the PNA and PSA pattern responses to enhanced equatorial convection (see Figure 3-3 of Chen 2005). In the wave train, ascending motion and cooling occur in low pressure cyclonic regions, and the opposite in high pressure regions. The SST change is delayed relative to the atmosphere

change by the larger thermal inertia of the ocean but has the same sign (Alexander 2002), because Ekman transport associated with the cyclonic flow results in upwelling and a shoaling thermocline, and increased storminess intensifies ocean mixing and heat flux to the atmosphere (Deser et al. 1996).

In the Northeast Pacific, there is a narrow region in which the ST appears to lead N34h, but the ECLL is small here and has little effect on the ENSO removal technique described below. Near the west coast of Chile and Peru, ST also leads N34h, and here ECLL is high. This precursor feature has been mentioned by Rasmusson and Carpenter (1982). Enfield and Mestas-Nunez (1999) attribute it to a surface heat flux change due to weaker trade winds off the Chilean coast, which precede the main Pacific trade wind weakening. Centered on the Maritime Continent, three regions in which ST leads N34h, extend to the north, west, and southeast. These have been observed also by Trenberth (2002).

ST over the Indian Ocean and South China Sea highly correlate with N34h at about 2 - 6 months lag (Lanzante 1996; Enfield and Mestas-Nunez 1999). El Niño causes anomalous subsidence there that reduces cloud amount; thus, more solar radiation reaches the surface and warms the ocean but with a delay due to its large thermal inertia. The smaller lag in the Indian Ocean is attributed to the fact that cloud changes in the Indian Ocean lead the ENSO index by three months due to the altered summer monsoons (Webster and Yang 1992; Lau and Yang 1996). In the South China Sea, the change in cloud amount coincides with the ENSO index (Klein et al. 1999).

In the tropical Atlantic Ocean, ST lags N34h by about 5 - 6 months (Lanzante 1996). The local Hadley cell weakens during El Niño, manifesting in a negative (positive)

anomalous change near the intertropical convergence zone (in the subtropics) in water vapor, cloud amount, and reflected SW flux, although the surface latent heat flux change due to weakened trade winds seems more important in the tropical North Atlantic (Enfield and Mayer 1997; Klein et al. 1999; Alexander et al. 2002). In part of the Gulf of Guinea, ST anticorrelates with N34h, leading it by about 6 months. This feature is also consistent with Trenberth (2002), although the reasons have not been addressed.

c. ENSO removal method

Because most of the lag and ECLL features in Figure A2 can be explained by known ENSO and teleconnection mechanisms, the N34h index and the ECLL relationship between the N34h index and a given climate parameter provide a good approximate description of the ENSO effect on that parameter. Based on this, we can roughly remove the ENSO signal at the grid box level from the spatiotemporal field of that parameter. We first calculate the ECLL between N34h and the anomalies of climate parameter T at each grid box. For example, at grid box *i*, we obtain $ECLL_i$ at lag *j*. Negative lag means that the N34h index leads the climate parameter for |*j*| months. We calculate the standard deviation of N34h, denoted as σ_{N34h}, and the standard deviation of T_i, denoted as σ_{T_i}. The residual value of T with ENSO-removed at grid box *i* and time *m*, denoted as $Tres_{i,m}$, is then calculated as follows:

$$Tres_{i,m} = T_{i,m} - N34h_{m+j} \times ECLL_i \times \sigma_{T_i} / \sigma_{N34h}$$

In the above equation, the second term of the right side is the regression of T onto the N34h index for the least lag at which the extreme cross-correlation magnitude between T and N34h occurs. The removal procedure is applied only to grid boxes where $ECLL_i$ is

statistically significant above the 99% confidence level.

This ENSO-removal method is tested with the cross-correlations for a ±12 months lag range between the N34h index and the principal component (PC) time series of the EOF analyses, based on GISTEMP and ERSST.V2 with or without the ENSO-removal procedure. In the EOF analyses of the original data (Figure 3.6 in Chen 2005), the principal components of the first few modes significantly correlate with N34h at different lags. However, none of the principal components from the ENSO-removed data significantly correlate with the N34h index at any lag. In both the GISTEMP and ERSST.V2 ENSO-removed annually smoothed EOF analyses, the first two modes clearly represent global warming and the pan-decadal variability in the Pacific, respectively. The fact that these long-term climate variations emerge after the ENSO signal is removed suggests that the removal method is successful. The technique has also successfully been applied to extract known ENSO features in satellite precipitation datasets (Chen et al. 2007b).

The ENSO-removal method is based on the broadly accepted assumptions that the ENSO phenomenon can be represented by the N34h index and that stable global linear lag relationships exist between N34h and climate parameters. However, we note that global lag relationships between the N34h index and the climate parameters can be modified when the climate background is shifted. For example, in Figure 3-7 of Chen (2005), the lag relationships are compared before and after the 1976 climate shift. In the period 1958 to 1975, the equatorial East Pacific leads the Central Pacific; from 1979 to 1996, the equatorial East Pacific lags the Central Pacific. Trenberth et al. (2002) hypothesize that a shift in the balance of terms within the ocean associated with the 1976

climate shift in the equatorial Pacific may have caused the change, but Wang and An (2002) attribute it to equatorial winds and an associated upwelling change after 1976. In addition, although ENSO and its effect on remote regions can be explained mostly based on linear dynamics, nonlinearity also plays a role (Trenberth et al. 1998), and asymmetry between warm and cold events needs to be considered (Larkin and Harrison 2002) in the future.

Appendix B. Effects of Data discontinuities on Reanalyses

The reliability of reanalysis products for estimating long-term climate trends is considered here. Although there are deficiencies in the reanalysis models (Bony et al. 1997), the fixed model strategy and constraints from the assimilated observations cause parameters with relatively more observations to be less affected by model problems. But because the model has inherent biases and the system is forced to fit the assimilated observations, changes in the observation system can introduce artificial climate change. The global observation system has experienced two major changes: the global radiosonde network established in 1958 and the global operational satellite observation system established in the 1970s (Kistler et al. 2001).

Several studies indicate weaknesses of the reanalysis products for global climate change studies. Kistler et al. (2001) address the fact that the NCEP/NCAR data pre-1958 have poorer quality and that the effect of the introduction of the global satellite observation system in 1979 is largest at or above 200hPa and south of 60°S. Discrepancies in the lower stratosphere and upper troposphere before and after 1979 are caused by biases from both the NCEP model and NESDIS retrievals (Santer et al. 1999). Sturaro (2003) finds that the 1979 spurious shifts in the temperature fields are broader than earlier estimates: the largest changes occurred near 100hPa, but the affected regions include the tropics between 700 and 50hPa and the southern ocean region between 500 and 250hPa. In Kinter et al. (2004), discrepancies in precipitation time series between observations and reanalysis in several tropical regions are attributed to the problematic divergent circulation in the reanalysis.

Through EOF analysis applied to individual or combined parameter fields in different

time ranges, we find that suspicious climate variations occur in earlier reanalysis data, especially before the 1970s. We also find that the effect of the 1979 discontinuity can be reduced if we add a large number of parameter fields to the combined EOF analysis. This is understandable because the essence of the EOF analysis is to draw the greatest possible commonality from the parameter fields sequentially under the orthogonal constraint. The impact of the 1979 discontinuity differs among parameters, geographical locations and pressure levels (Sturaro 2003). So if we exclude the most affected regions, above 300hPa and high latitudes, then the commonality of the data fields (i.e., the real climate variation) should emerge as the dominant mode of the combined EOF analysis.

A quantitative analysis of the discontinuities in the reanalysis data determines how successful this approach is in suppressing them. The discontinuity testing algorithm is based on the work of Rodionov (2004). This method is used to sequentially test the validity of a null hypothesis (in this case, the existence of discontinuity) for each value in a time series. If a value in the time series exceeds a criterion range, which is decided based on the l values earlier than the test value with the student's t-test method, then a regime shift index (RSI, which is a cumulative sum of the normalized anomalies relative to the range limit of the l values after the test point) at this test point is calculated. If the RSI becomes negative during the calculation, then the hypothesis is rejected, and the RSI is set back to zero. If the RSI remains positive, then the discontinuity at the test point is significant at the probability level set with the Student's t-test. With this algorithm, we can obtain a discontinuity time series corresponding to a given time series. The discontinuity time series has the same time length as the original time series. In the discontinuity time series, a value of zero indicates that no discontinuity has occurred at

that point, and a positive value indicates that a discontinuity has occurred. The value itself represents the strength of the discontinuity.

To obtain a general picture of the discontinuities in the reanalyses, we calculate the discontinuity time series for each grid box of the five parameters at each pressure level in the troposphere (1000hPa-100hPa) from 1948 (NCEP/NCAR) and 1958 (ERA-40). Figure B1 shows the mean discontinuity time series for each parameter of the two reanalyses. For NCEP/NCAR, discontinuities of T_{air} have almost double the range of strength compared with those of the other four parameters. Discontinuities for all parameters are relatively large before 1958. For U, V, ω, and q, discontinuities are relatively small after 1970 except during the 1974 to 1980 period. Discontinuities in the ERA-40 dynamical fields are comparable to that of NCEP/NCAR, and the ERA-40 q (T_{air}) has more (fewer) high discontinuity values than its counterpart in NCEP/NCAR.

These discontinuities, especially around January 1979, are considered to be an obstacle to using reanalysis data in climate research (Chelliah and Ropelewski 2000; Sturaro 2003) due to the impact from the introduction of TOVS data. Figure B2 shows the zonal mean of the averaged discontinuity index from January 1978 to December 1979 for the five parameters in the vertical-meridional plane. NCEP/NCAR T_{air} shows more than double the discontinuity value of the other four parameters in NCEP/NCAR. For all parameters except q, the discontinuity maximum occurs at 100hPa in the tropics. The maximum discontinuity in T_{air} at 100hPa extends to 200hpa in the tropics; the maximum is around 300hPa in the Southern Hemisphere; and there is also a weak local tropical maximum at 700hPa and 850hPa.

In the three NCEP/NCAR dynamical parameter plots, discontinuities are relatively

small compared to the T_{air}, but there are extreme regions around 60°S throughout the troposphere for V and ω. Discontinuities in q have the same strength as those in the dynamical parameters, and the maximum occurs in the tropics at 300hPa. This is the highest level for this parameter, but there are extremes near the surface around the equator and at 60°S. From the above plots, it is clear that the 1979 discontinuity is unevenly distributed. Excluding data above the 300hPa level eliminates much of the discontinuity problem. The middle to high latitudes in the Southern Hemisphere have a stronger discontinuity signal than other latitudes. In order to weaken the effect of the 1979 discontinuity, the analysis latitude range is confined to 60S-60N. Other significant discontinuity features located at lower altitude (latitude) regions cannot be easily avoided and must be considered when interpreting results in the main text.

The ERA-40 has different discontinuity patterns, but these discontinuities are also not evenly distributed in space and among different parameters. Shown in the left column of Figure B2, strong discontinuities are located at high latitude in T_{air}, q, and ω. In the middle latitudes of the Southern Hemisphere, there is a strong discontinuity in q.

To determine how the introduction of satellite data around 1979 affects EOF analysis, we conducted an experiment based on the NCEP/NCAR reanalysis. First, EOF analysis was performed individually on each of the five parameters at each of the eight levels from 1000hPa to 300hPa for 60°S-60°N from 1948 to 2001. We then calculated the discontinuity time series corresponding to the first 10 principal component (PC) time series for each EOF analysis. The mean discontinuity values from January 1978 to December 1979 corresponding to the PCs are shown in Figure 4-4 of Chen (2005). For T_{air}, except at 1000hPa, the 1979 discontinuity appears in all first mode PCs. For q, the

1979 discontinuity appears in the first two modes at 400hPa, 500hPa, 600hPa, and 850hPa. For U, the 1979 discontinuity appears in the first two modes at 500hPa, 600hPa and 850hPa. For V, there is no sign of the 1979 discontinuity in the first two modes. For ω, the 1979 discontinuity appears in the first two modes at 300hPa, 400hPa and 700hPa.

The 1979 discontinuity problem is largely overcome by a single combined EOF analysis for all five parameters at all eight pressure levels. In the combined EOF analysis for 1948 to 2001, a weak discontinuity appears in the second mode PC around 1979. Beside the 1979 discontinuity, strong suspicious variability appears in the second and third PCs early in the time period. In the analysis based on the 1970 to 2001 period, no discontinuity appears in the first four mode PCs around 1979. Thus, the combined EOF analysis can indeed suppress the 1979 discontinuity, because this discontinuity is not coherently distributed in reanalysis parameters.

.

References:

Alexander, M.A., I. Blade, M. Newman, J.R. Lanzante, N.C. Lau and J.D. Scott, 2002: The atmospheric bridge: The influence of ENSO teleconnections on air-sea interaction over the global oceans. *J. Clim.* **15**: 2205-2231.

Bengtsson, L., S. Hagemann, and K.I. Hodges, 2004a: Can climate trends be calculated from reanalysis data? *J. Geophys. Res.-Atmos.* **109**: D11111, doi:10.1029/2004JD004536

Bengtsson, L., K.I. Hodges, and S. Hagemann, 2004b: Sensitivity of large-scale atmospheric analyses to humidity observations and its impact on the global water cycle and tropical and extratropical weather systems in ERA40. *Tellus* **56**: 202-217.

Bjerknes, J, 1969: Atmospheric teleconnections from equatorial pacific. *Mon. Weather Rev.* **97**: 163-172.

Bony, S., Y. Sud, K.M. Lau, J. Susskind and S. Saha., 1997: Comparison and satellite assessment of NASA/DAO and NCEP-NCAR reanalyses over tropical ocean: Atmospheric hydrology and radiation. *J. Clim.*, **10**: 1441-1462.

Cai M. and E. Kalnay., 2005: Can reanalysis have anthropogenic climate trends without model forcing? *J. Clim.*, **18**: 1844-1849.

Callendar, G.S. (1938). "The Artificial Production of Carbon Dioxide and Its Influence on Climate." *Quarterly J. Royal Meteorological Society* **64**: 223-40.

Carleton, A.M, 2003: Atmospheric teleconnections involving the Southern Ocean. *J. Geophys. Res.-Oceans* **108**.

Chelliah M., C.F. Ropelewski, 2000: Reanalysis-based tropospheric temperature estimates: uncertainties in the context of global climate change detection. *J. Clim.*, **13**: 3187–3205.

Chen, J., 2005: Understanding the observed tropical and mid-latitude radiative energy budget in the context of long-term climate variations. Ph.D. Dissertation, Columbia University.

Chen J., A.D. Del Genio, B.E. Carlson, M.G. Bosilovich, 2007a: The spatiotemporal structure of 20th century climate variations in observations and reanalyses. Part II: Pacific pan-decadal variability. *J. Clim.*, submitted.

Chen Y., A.D. Del Genio, J. Chen 2007b: The Tropical atmospheric El Niño Signal in satellite precipitation data and a global climate model. *J. Clim.*, **20**, 3580-3601.

Chiang, J.C.H. and A.H. Sobel, 2002: Tropical tropospheric temperature variations caused by ENSO and their influence on the remote tropical climate. *J. Clim.*, **15**: 2616-2631.

Cubasch, U., G.A. Meehl and Coauthors, 2001: Projections of Future Climate Change. *Climate Change 2001: The Science Basis,* J. T. Houghton et al., Eds., Intergovernmental Panel on Climate Change, Cambridge University Press, 525-582.

Deser, C., M.A. Alexander and M.S. Timlin, 1996: Upper-ocean thermal variations in the North Pacific during 1970-1991. *J. Clim.*, **9**: 1840-1855.

Ellsaesser, H.W., M.C. McCracken, J.J. Walton, and S.L. Grotch, 1986: Global climatic trends as revealed by the recorded data. *Rev. Geophys.*, **24**: 745-792.

Enfield, D.B. and D.A. Mayer, 1997: Tropical Atlantic sea surface temperature variability and its relation to El Niño Southern Oscillation. *J. Geophys. Res.-Oceans* **102**: 929-945.

Enfield, D.B. and A.M. Mestas-Nunez, 1999: Multiscale variabilities in global sea surface temperatures and their relationships with tropospheric climate patterns. *J. Clim.* **12**: 2719-2733.

Folland, C.K., T.R. Karl and Coauthors, 2001: Observed Climate Variability and Change. *Climate Change 2001: The Science Basis,* J. T. Houghton et al., Eds., Intergovernmental Panel on Climate Change, Cambridge University Press, 99-182.

Folland, C.K., D. Parker, R.W. Reynolds, S.C. Sherwood, P.W. Thorne, 2006: What measures can be taken to improve the understanding of observed changes? in *Temperature Trends in the Lower Atmosphere: Steps for Understanding and Reconciling Differences*. T. R. Karl, S. J. Hassol, C. D. Miller, and W. L. Murray, editors. A Report by the Climate Change Science Program and the Subcommittee on Global Change Research, Washington, DC.

Fu, R., W.T. Liu and R.E. Dickinson, 1996: Response of tropical clouds to the interannual variation of sea surface temperature. *J. Clim.* **9**: 616-634.

Gordon, A.L., 2001: Interocean Exchange. *Ocean Circulation & Climate: Observing and Modelling the Global Ocean,* G. Siedle et al., Eds., Academic Press, 303-313.

Hanley, D.E., M.A. Bourassa, J.J. O'Brien, S.R. Smith and E.R. Spade, 2003: A quantitative evaluation of ENSO indices. *J. Climate* **16**: 1249-1258.

Hansen, J.E., and S. Lebedeff, 1987: Global trends of measured surface air temperature. *J. Geophys. Res.*, **92**: 13345-13372.

Hansen, J.E., M. Sato, A. Lacis, R. Ruedy, I. Tegen, and E. Matthews, 1998: Climate forcings in the industrial era. *Proc. Natl. Acad. Sci.*, **95**: 12,753–12,758.

Hansen, J., R. Ruedy, J. Glascoe and M. Sato., 1999: GISS analysis of surface temperature change. *J. Geophys. Res.-Atmos.*, **104**: 30997-31022.

Hansen, J., M. Sato, L. Nazarenko, R. Ruedy, A. Lacis, D. Koch, I. Tegen, T. Hall, D. Shindell, B. Santer, P. Stone, T. Novakov, L. Thomason, R. Wang, Y. Wang, D. Jacob, S. Hollandsworth, L. Bishop, J. Logan, A. Thompson et al., 2002: Climate forcings in Goddard Institute for Space Studies SI2000 simulations. *J. Geophys. Res.-Atmos.* **107**, doi: 10.1029/2001JD001143.

Harrison, D.E. and N.K. Larkin, 1998: El Niño-Southern Oscillation sea surface temperature and wind anomalies, 1946-1993. *Rev. Geophys.* **36**: 353-399.

Haywood, J.M., D.L. Roberts, A. Slingo, J. M. Edwards, and K. P. Shine, 1997: General circulation model calculations of the direct radiative forcing by anthropogenic sulphate and fossil-fuel soot aerosol. *J. Clim.*, **10**: 1562–1577.

Hegerl, G.C., F.W. Zwiers and Co-Authors, 2007: Understanding and attributing climate change. In: *Climate Change 2007: The Physical Science Basis. Contribution of Working Group 1 to the Fourth Assessment Report of the Intergovernmental Panel on Climate Change* [Solomon, S., et al. (eds.)]. Cambridge University Press, Cambridge, United Kingdom and New York, NY USA.

Horel, J.D. and J.M. Wallace, 1981: Planetary-scale atmospheric phenomena associated with the Southern Oscillation. *Mon. Weather Rev.* **109**: 813-829.

Hoskins, B.J. and D.J. Karoly, 1981: The steady linear response of a spherical atmosphere to thermal and orographic forcing. *J. Atmos. Sci.* **38**: 1179-1196.

Jones, P. D., The influence of ENSO on global temperatures, *Clim. Monitor*, 17, 80-89, 1988

Jones, P.D., M. New, D.E. Parker, S. Martin and I.G. Rigor., 1999: Surface air temperature and its changes over the past 150 years. *Rev. Geophys.*, **37**: 173-199.

Kalnay, E., M. Kanamitsu, R. Kistler, W. Collins, D. Deaven, L. Gandin, M. Iredell, S. Saha, G. White, J. Woollen, Y. Zhu, M. Chelliah, W. Ebisuzaki, W. Higgins, J. Janowiak, K.C. Mo, C. Ropelewski, J. Wang, A. Leetmaa and R. Reynolds.,1996: The NCEP/NCAR 40-year reanalysis project. *Bull. Amer. Meteorol. Soc.*, **77**: 437-471.

Karl, T.R., R.W. Knight, G. Kukla, and G. Gavin, 1995: Evidence for the radiative effects of anthropogenic sulfate aerosols in the observed climatic record. *Aerosol Forcing of Climate*, R. Charlson and J. Heintzenberg, Eds., John Wiley, 363-382.

Karl, T.R., S.J. Hassol, C.D. Miller, and W.L. Murray, editors, 2006: Temperature Trends in the Lower Atmosphere: Steps for Understanding and Reconciling Differences. *A Report by the Climate Change Science Program and the Subcommittee on Global Change Research, Washington, DC.*

Kelly, P.M. and P.D. Jones, 1996: Removal of the El Niño Southern Oscillation signal from the gridded surface air temperature data set. *J. Geophys. Res.-Atmos.* **101**: 19013-19022.

Kinter, J.L., M.J. Fennessy, V. Krishnamurthy and L. Marx, 2004: An evaluation of the apparent interdecadal shift in the tropical divergent circulation in the NCEP-NCAR reanalysis. *J. Clim.*, **17**: 349-361.

Kistler, R., E. Kalnay, W. Collins, S. Saha, G. White, J. Woollen, M. Chelliah, W. Ebisuzaki, M. Kanamitsu, V. Kousky, H. van den Dool, R. Jenne and M. Fiorino, 2001: The NCEP-NCAR 50-year reanalysis: Monthly means CD-ROM and documentation. *Bull. Amer. Meteorol. Soc.*, **82**: 247-267.

Klein, S.A., B.J. Soden and N.C. Lau, 1999: Remote sea surface temperature variations during ENSO: Evidence for a tropical atmospheric bridge. *J. Clim.* **12**: 917-932.

Lanzante, J.R, 1996: Lag relationships involving tropical sea surface temperatures. *J. Clim.* **9**: 2568-2578.

Lanzante, J.R., T.C. Peterson, F.J. Wentz, K.Y. Vinnikov, 2006: What do observations indicate about the change of temperatures in the atmosphere and at the surface since the advent of measuring temperatures vertically? in *Temperature Trends in the Lower Atmosphere: Steps for Understanding and Reconciling Differences*. T. R. Karl, S. J. Hassol, C. D. Miller, and W. L. Murray, editors. A Report by the Climate Change Science Program and the Subcommittee on Global Change Research, Washington, DC.

Larkin, N.K. and D.E. Harrison, 2002: ENSO warm (El Niño) and cold (La Nina) event life cycles: Ocean surface anomaly patterns, their symmetries, asymmetries, and implications. *J. Clim.* **15**: 1118-1140.

Lau, K.M. and S. Yang, 1996: The Asian monsoon and predictability of the tropical ocean-atmosphere system. *Q. J. R. Meteorol. Soc.* **122**: 945-957.

Lau, N.C. and M.J. Nath, 1996: The role of the "atmospheric bridge" in linking tropical Pacific ENSO events to extratropical SST anomalies. *J. Clim.* **9**: 2036-2057.

Lau, N.C, 1997: Interactions between global SST anomalies and the midlatitude atmospheric circulation. *Bull. Amer. Meteorol. Soc.* **78**: 21-33.

Levitus, S., J.I. Antonov, T.P. Boyer and C. Stephens, 2000: Warming of the World Ocean. *Science*, **287**: 2225-2229.

Mann, M.E., R.S. Bradley, and M.K. Hughes, 1999: Northern Hemisphere Temperatures During the Past Millennium: Inferences, Uncertainties, and Limitations. *Geophys. Res. Lett.*, **26**: 759-762.

Mitas, C.M. and A. Clement, 2005: Has the Hadley cell been strengthening in recent decades? *Geophys. Res. Lett.*, **32**: L03809, doi:10.1029/2004GL021765.

Mitas, C.M. and A. Clement, 2006: Recent behavior of the Hadley cell and tropical thermodynamics in climate models and reanalyses. *Geophys. Res. Lett.*, **33**: L01810, doi:10.1029/2005GL024406.

Mitchell, J. and T.C. Johns, 1997: On modification of global warming by sulfate aerosols. *J. Clim.*, **10**: 245-267.

Neelin, J.D., D.S. Battisti, A.C. Hirst, F.F. Jin, Y. Wakata, T. Yamagata and S.E. Zebiak, 1998: ENSO theory. *J. Geophys. Res.-Oceans* **103**: 14261-14290.

Opsteegh, J.D. and H.M. Vandendool, 1980: Seasonal differences in the stationary response of a linearized primitive equation model - prospects for long-range weather forecasting. *J. Atmos. Sci.* **37**: 2169-2185.

Penland, C. and Matrosova L., 2006: Studies of El Niño and interdecadal variability in tropical sea surface temperatures using a nonnormal filter. *J. Clim.*, **19**: 5796-5815.

Penner, J.E., C.C. Chuang, and K. Grant, 1998: Climate forcing by carbonaceous and sulfate aerosols. *Clim. Dyn.*, **14**: 839–851.

Privalsky, V.E. and D.T. Jensen, 1995: Assessment of the influence of ENSO on annual global air temperatures. *Dyn. Atmos. Oceans* **22**: 161-178.

Rasmusson, E.M. and T.H. Carpenter, 1982: Variations in tropical sea-surface temperature and surface wind fields associated with the Southern Oscillation El-niño. *Mon. Weather Rev.* **110**: 354-384.

Rayner, N.A., D.E. Parker, E.B. Horton, C.K. Folland, L.V. Alexander, D.P. Rowell, E.C. Kent, and A. Kaplan, 2003: Global analyses of sea surface temperature, sea ice, and night marine air temperature since the late nineteenth century, *J. Geophys. Res.* **108:** D14, 4407, doi:10.1029/2002JD002670.

Reynolds, R.W., N.A. Rayner, T.M. Smith, D.C. Stokes and W.Q. Wang, 2002: An improved in situ and satellite SST analysis for climate. *J. Clim.* **15**: 1609-1625.

Robock, A. and J.P. Mao, 1995: The volcanic signal in surface-temperature observations. *J. Clim.* **8**: 1086-1103.

Rodionov, S. N., 2004: A sequential algorithm for testing climate regime shifts. *Geophys. Res. Lett.*, **31**, doi:10.1029/2004GL019448.

Santer, B.D., J.J. Hnilo, T. Wigley, J.S. Boyle, C. Doutriaux, M. Fiorino, D.E. Parker and K.E. Taylor, 1999: Uncertainties in observationally based estimates of temperature change in the free atmosphere. *J. Geophys. Res.-Atmos.*, **104**: 6305-6333.

Santer, B.D., T. Wigley, C. Doutriaux, J.S. Boyle, J.E. Hansen, P.D. Jones, G.A. Meehl, E. Roeckner, S. Sengupta and K.E. Taylor, 2001: Accounting for the effects of volcanoes and ENSO in comparisons of modeled and observed temperature trends. *J. Geophys. Res.-Atmos.,* **106**: 28033-28059.

Santer, B.D., T.M.L. Wigley, A.J. Simmons, P.W. Kållberg, G.A. Kelly, S.M. Uppala, C. Ammann, J.S. Boyle, W. Brüggemann, C. Doutriaux, M. Fiorino, C. Mears, G.A. Meehl, R. Sausen, K.E. Taylor, W.M. Washington, M.F. Wehner, and F.J. Wentz, 2004: Identification of anthropogenic climate change using a second-generation reanalysis. *Journal Geophy. Res.-Atmos.*, **109**, D21104, doi:10.1029/2004JD005075.

Santer, B.D., J.E. Penner, and P.W. Thorne, 2006: How well can the observed vertical temperature changes be reconciled with our understanding of the causes of these changes? in *Temperature Trends in the Lower Atmosphere: Steps for Understanding and Reconciling Differences*. T. R. Karl, S. J. Hassol, C. D. Miller, and W. L. Murray, editors. A Report by the Climate Change Science Program and the Subcommittee on Global Change Research, Washington, DC.

Scaife, A.A., J.R. Knight, G.K. Vallis, and C.K. Folland, 2005: A stratospheric influence on the winter NAO and North Atlantic surface climate. *Geophys. Res. Lett.*, **32**, L18715, doi:10.1029/2005GL023226.

Schneider, T. and I.M. Held, 2001: Discriminants of twentieth-century changes in earth surface temperatures. *J. Clim.*, **14**: 249-254.

Slutz, R.J., S.J. Lubker, J.D. Hiscox, S.D. Woodruff, R.L. Jenne, D.H. Joseph, P.M. Steurer, and J.D. Elms, 1985: *Comprehensive Ocean-Atmosphere Data Set; Release 1*. NOAA Environmental Research Laboratories, Climate Research Program, Boulder, CO, 268 pp. (NTIS PB86-105723).

Smith, T.M. and R.W. Reynolds, 2003: Extended reconstruction of global sea surface temperatures based on COADS data (1854-1997). *J. Clim.* **16**: 1495-1510.

Smith, T.M. and R.W. Reynolds, 2004: Improved Extended Reconstruction of SST (1854-1997). *J. Clim.* **17**: 2466-2477.

Song, Q., A.L. Gordon and M. Visbeck, 2004: Spreading of the Indonesian throughflow in the Indian Ocean. *J. Phys. Oceanogr.*, **34**: 772-792.

Sturaro, G., 2003: A closer look at the climatological discontinuities present in the NCEP/NCAR reanalysis temperature due to the introduction of satellite data. *Clim. Dyn.*, **21**: 309-316.

Susanto, R.D. and A.L. Gordon, 2005: Velocity and transport of the Makassar Strait throughflow. *J. Geophys. Res.* **110**, C01005, doi:10.1029/2004JC002425

Tegen, I., A. Lacis, and I. Fung, 1996: The influence of mineral aerosols from disturbed soils on climate forcing. *Nature*, **380**, 419–422.

Trenberth, K.E., G.W. Branstator, D. Karoly, A. Kumar, N.C. Lau and C. Ropelewski, 1998: Progress during TOGA in understanding and modeling global teleconnections associated with tropical sea surface temperatures. *J. Geophys. Res.-Oceans* **103**: 14291-14324.

Trenberth, K.E., J.M. Caron, D.P. Stepaniak and S. Worley, 2002: Evolution of El Nino-Southern Oscillation and global atmospheric surface temperatures. *J. Geophys. Res.-Atmos.* **107, D8**, doi:10.1029/2000JD000298.

Trenberth, K.E., L. Smith, 2005: The mass of the atmosphere: a constraint on global analyses. *J Clim.* **18**: 86–875.

Trenberth, K.E., J. Fasullo, L. Smith, 2005: Trends and variability in column-integrated atmospheric water vapor. *Clim. Dyn.* **24**: 741-758.

Trenberth, K.E.,, P.D. Jones and Co-Authors, 2007: Observations: Surface and atmospheric climate change. In: *Climate Change 2007: The Physical Science Basis. Contribution of Working Group 1 to the Fourth Assessment Report of the Intergovernmental Panel on Climate Change* [Solomon, S., et al. (eds.)]. Cambridge University Press, Cambridge, United Kingdom and New York, NY USA.Uppala, S.M., P.W. Kållberg, A.J. Simmons, U. Andrae V. da Costa Bechtold, M. Fiorino, J.K. Gibson, J. Haseler, A. Hernandez, G.A. Kelly, X. Li, K. Onogi, S. Saarinen, N. Sokka, R.P. Allan, E. Andersson, K. Arpe, M.A. Balmaseda, A.C.M. Beljaars, L. van de Berg, J. Bidlot, N. Bormann, S. Caires, F. Chevallier, A. Dethof, M. Dragosavac, M. Fisher, M. Fuentes, S. Hagemann, E. Hólm, B.J. Hoskins, L. Isaksen, P.A.E.M. Janssen, R. Jenne, A.P. McNally, J.-F. Mahfouf, J.-J. Morcrette, N.A. Rayner, R.W. Saunders, P. Simon, A. Sterl, K.E. Trenberth, A. Untch, D. Vasiljevic, P. Viterbo, and J. Woollen, 2005: The ERA-40 re-analysis. *Quart. J. R. Meteorol. Soc.*, 131: 2961-3012. doi:10.1256/qj.04.176

Wallace, J.M., E.M. Rasmusson, T.P. Mitchell, V.E. Kousky, E.S. Sarachik and H. von Storch, 1998: The structure and evolution of ENSO-related climate variability in the tropical Pacific: Lessons from TOGA. *J. Geophys. Res.-Oceans* **103**: 14241-14259.

Wang, B. and S.I. An, 2002: A mechanism for decadal changes of ENSO behavior: roles of background wind changes. *Clim. Dyn.* **18**: 475-486.

Weart, S.R., 2003: The Discovery of Global Warming, Harvard University Press.

Webster, P.J. and S. Yang, 1992: Monsoon and ENSO - selectively interactive systems. *Q. J. R. Meteorol. Soc.* **118**: 877-926.

Webster, P.J., 1981: Mechanisms determining the atmospheric response to sea-surface temperature anomalies. *J. Atmos. Sci.* **38**: 554-571.

Worley, S.J., S.D. Woodruff, R.W. Reynolds, S.J. Lubker, and N. Lott, 2005: ICOADS Release 2.1 data and products. *Int. J. Climatol. (CLIMAR-II Special Issue)*, **25**, 823-842 (DOI: 10.1002/joc.1166).

Zhang, Y., J.M. Wallace and D.S. Battisti, 1997: ENSO-like interdecadal variability: 1900-93. *J. Clim.* **10**: 1004-1020.

Figure Captions

Figure 1. The time series of the GW trend in the 60°S-60°N latitude band. Because the 60°S-60°N zonal band covers 86.6% of the earth's surface and a reliable long-term observation record is lacking in the polar regions, the average temperature for this zonal band is assumed to roughly represent the known average temperature of the entire area of the earth.

Orange solid: original anomaly mean based on GISTEMP; blue dot-dashed: ENSO-related anomaly mean; brown triangle up: ENSO-removed anomaly mean; red square: first mode principal component (PC) of GISTEMP ENSO-removed EOF, scaled to represent the mean temperature change associated with this mode; green circle: first mode principal component of ERSST.V2 ENSO-removed EOF, scaled to represent the mean temperature change associated with this mode.

Figure 2. The spatial patterns of the trend (first) modes of the 1900–2003 ENSO-removed EOF analyses based on GISTEMP and ERSST.V2. This mode explains 27.3% and 31.1% of the total variance in the ENSO-removed annually smoothed anomaly data of GISTEMP and ERSST.V2, respectively. Top: the EOF spatial pattern from GISTEMP. Bottom: the EOF spatial pattern from ERSST.V2. Each grid of the EOF spatial patterns is scaled to represent the range of the local temperature change associated with the PC time series.

Figure 3. The PCs of the GW trend (first) mode of the ENSO-removed combined EOF analyses based on reanalyses data. Red solid: PC from 1970–2003 NCEP1-40p analysis, based on NCEP/NCAR data; this accounts for 16.6% of the total variance. Black dashed: PC from 1970-2002 ERA40-40p analysis, based on ERA-40 data; this accounts for

15.1% of the total variance. For reference, the 1970–2003 segments of the 1900-2003 ENSO-removed EOF analyses based on GISTEMP (orange square) and ERSST.V2 (green triangle up) are also shown. The correlation coefficients for every pair of the time series in this plot are all above 0.9.

Figure 4. The spatial patterns of T_{air} variation from 1000hPa to 300hPa associated with the GW trend mode. Left column: from NCEP1-40p analysis, based on NCEP/NCAR reanalysis data. Right column: from ERE40-40p analysis, based on ERA-40 reanalysis data.

Figure 5. The representative spatial patterns of the dynamic variation associated with GW trend mode. Left column: from NCEP1-40p analysis, based on NCEP/NCAR reanalysis data. Right column: from ERE40-40p analysis, based on ERA-40 reanalysis data. Top row: the 300hPa horizontal wind field (vectors) and divergence derived from wind field (color, red represents positive value, blue represents negative value); middle row: the 500hPa vertical velocity field, positive value means descending motion; bottom row: similar as top row, but for 850hPa.

Figure 6. The circulation changes (black vectors) associated with the GW trend mode in the zonal mean meridional-vertical cross section (upper row) and the 10S-10N meridional mean zonal-vertical cross section (lower row). Left column: from NCEP1-40p analysis, based on NCEP/NCAR reanalysis data. Right column: from ERE40-40p analysis, based on ERA-40 reanalysis data. The climatology is drawn in green vectors. In the upper plots, the horizontal component of the vectors is meridional wind with unit 1(m/s), and the vertical component of the vectors is negative ω with unit $-1/60$(hPa/s). In the lower plots, the horizontal component of the vectors is zonal wind with unit 1(m/s), and the vertical

component of the vectors is negative ω with unit –1/120(hPa/s). The arrow lengths of the vectors are scaled as shown on the top of each row.

Figure 7. The *q* variation at selected pressure levels from 1000hPa to 300hPa associated with the GW trend mode. Left column: from NCEP1-40p analysis, based on NCEP/NCAR reanalysis data. Right column: from ERE40-40p analysis, based on ERA-40 reanalysis data.

Figure A1. Black solid: The time series of the Niño-3.4 index, which is defined as the averaged SST anomaly in the equatorial Eastern Pacific region of 5˚N-5˚S and 170˚W-120˚W. It is calculated from ERSST.V2. Red dashed: 6-year high-pass filtered Niño-3.4 index (N34h), used the same filter as in Zhang et al. (1997). Green dot-dashed square: 6-year low-pass filtered Niño-3.4 index.

Figure A2. The map of extreme cross-correlations at the least lag (ECLL) of the N34h index with ST. Upper: the map of lags at which ECLL is found in ±12 month range. Negative value means the N34h index leads temperature. Lower: the values of ECLL. In these plots, only the values in the grids for which the ECLL confidence level exceeds 99% are shown.

Figure B1. The global, 1000hPa-100hPa averaged discontinuity (RSI index defined in Rodionov, 2004) index time series for five atmospheric parameters (T_{air}, U, V, ω and *q*) from NCEP/NCAR (black solid) and ERA-40 (red dashed) reanalyses.

Figure B2. The zonal mean discontinuity index averaged around 1979 (from January 1978 to December 1979) for five parameters from NCEP/NCAR (right column) and ERA-40 (left column). The parameters shown from top to bottom: T_{air}, Q U, V, ω. The

color bar shows the strength of the discontinuity; the horizontal axes are latitude, and the vertical axes are pressure level.

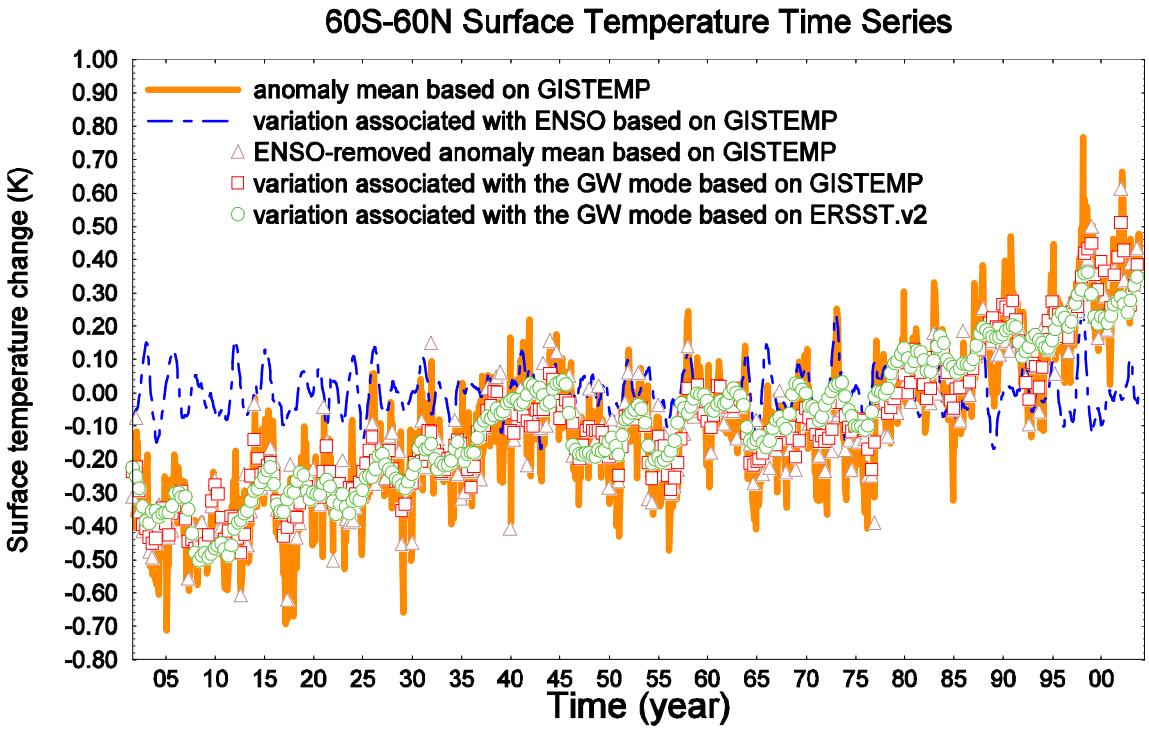

Figure 1. The time series of the GW trend in the 60°S-60°N latitude band. Because the 60°S-60°N zonal band covers 86.6% of the earth's surface and a reliable long-term observation record is lacking in the polar regions, the average temperature for this zonal band is assumed to roughly represent the known average temperature of the entire area of the earth.

Orange solid: original anomaly mean based on GISTEMP; blue dot-dashed: ENSO-related anomaly mean; brown triangle up: ENSO-removed anomaly mean; red square: first mode principal component (PC) of GISTEMP ENSO-removed EOF, scaled to represent the mean temperature change associated with this mode; green circle: first mode principal component of ERSST.V2 ENSO-removed EOF, scaled to represent the mean temperature change associated with this mode.

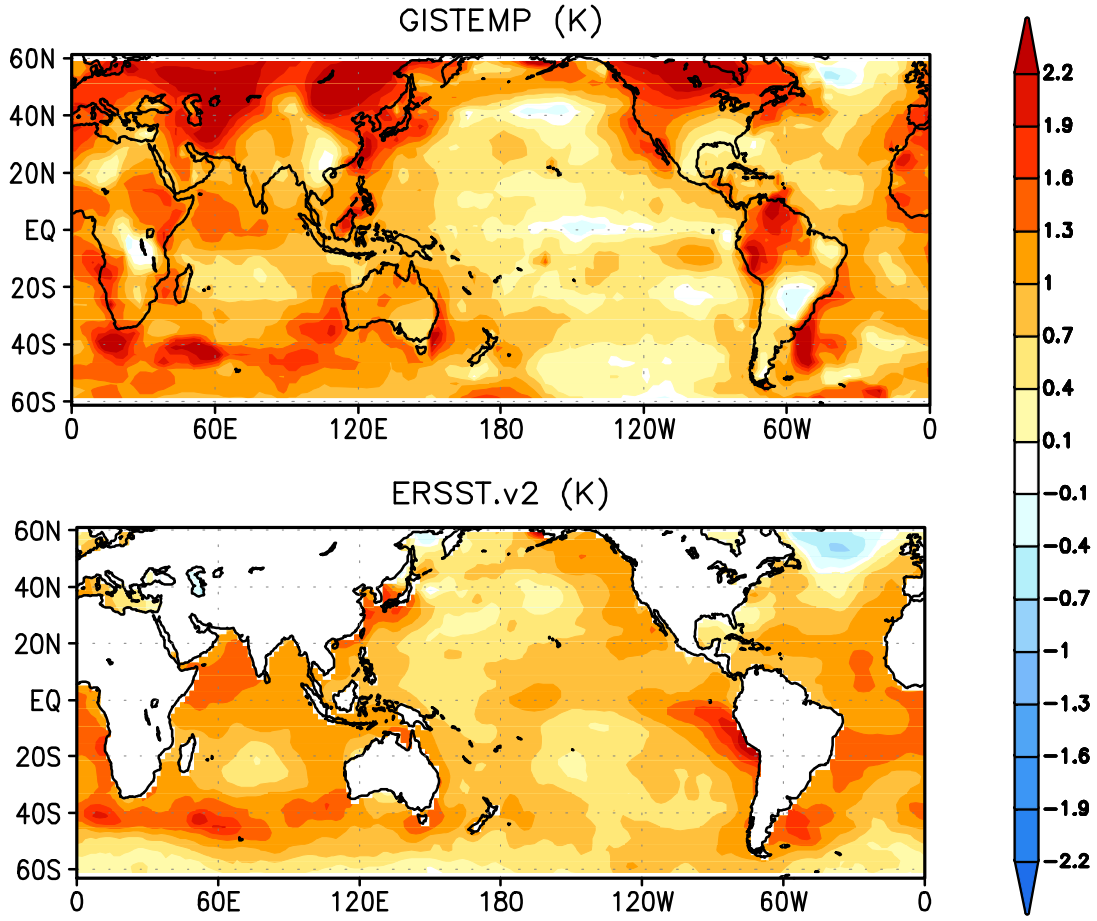

Figure 2. The spatial patterns of the trend (first) modes of the 1900–2003 ENSO-removed EOF analyses based on GISTEMP and ERSST.V2. This mode explains 27.3% and 31.1% of the total variance in the ENSO-removed annually smoothed anomaly data of GISTEMP and ERSST.V2, respectively. Top: the EOF spatial pattern from GISTEMP. Bottom: the EOF spatial pattern from ERSST.V2. Each grid of the EOF spatial patterns is scaled to represent the range of the local temperature change associated with the PC time series.

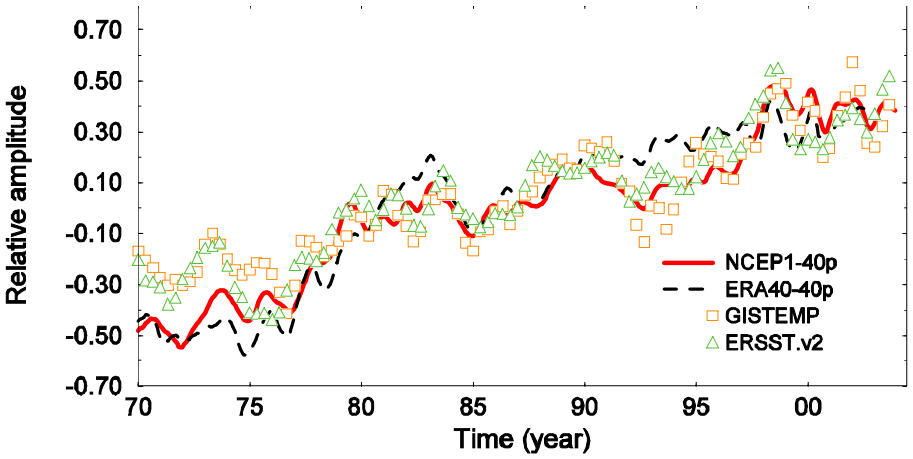

Figure 3. The PCs of the GW trend (first) mode of the ENSO-removed combined EOF analyses based on reanalyses data. Red solid: PC from 1970–2003 NCEP1-40p analysis, based on NCEP/NCAR data; this accounts for 16.6% of the total variance. Black dashed: PC from 1970-2002 ERA40-40p analysis, based on ERA-40 data; this accounts for 15.1% of the total variance. For reference, the 1970–2003 segments of the 1900-2003 ENSO-removed EOF analyses based on GISTEMP (orange square) and ERSST.V2 (green triangle up) are also shown. The correlation coefficients for every pair of the time series in this plot are all above 0.9.

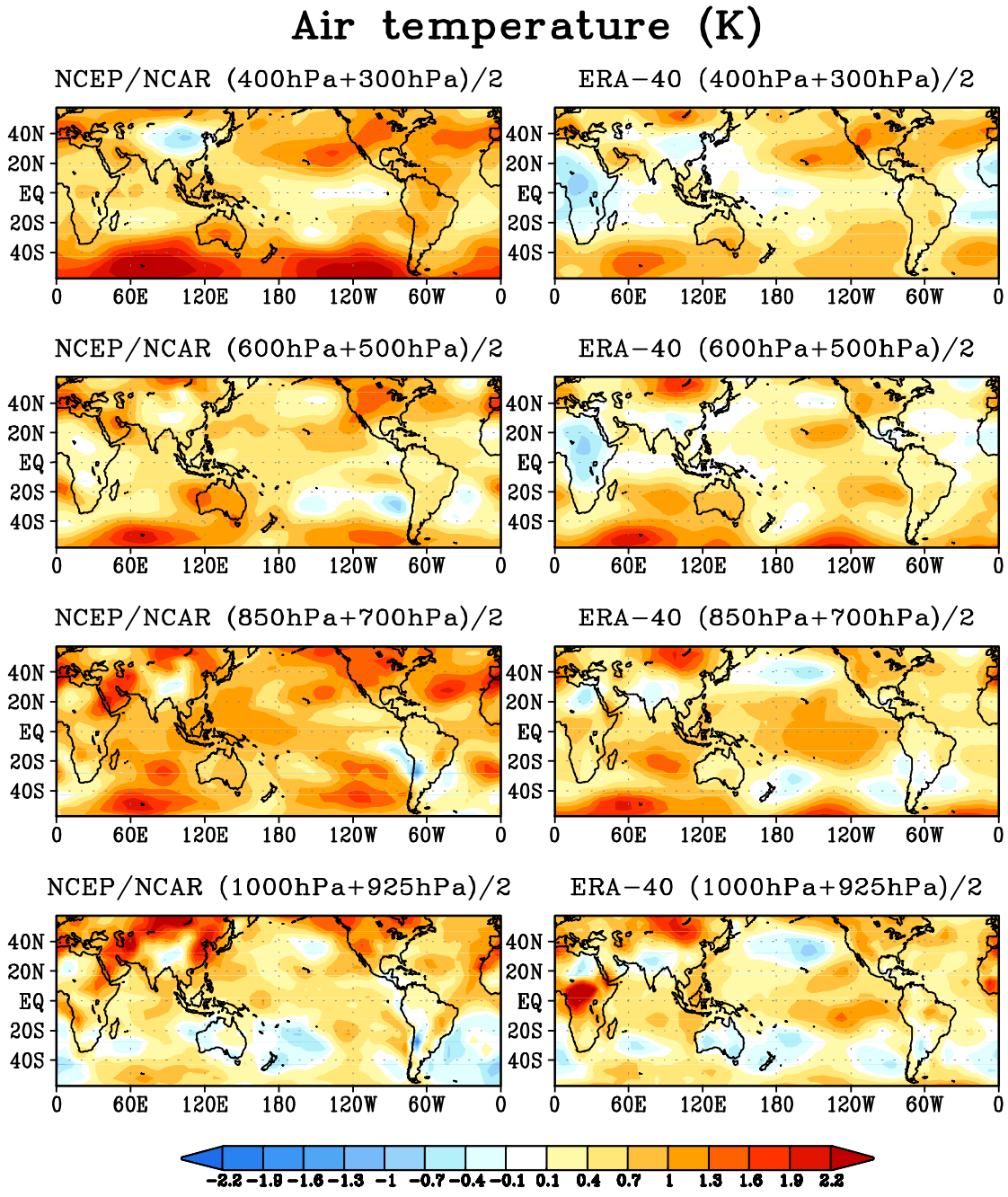

Figure 4. The spatial patterns of T_{air} variation from 1000hPa to 300hPa associated with the GW trend mode. Left column: from NCEP1-40p analysis, based on NCEP/NCAR reanalysis data. Right column: from ERE40-40p analysis, based on ERA-40 reanalysis data.

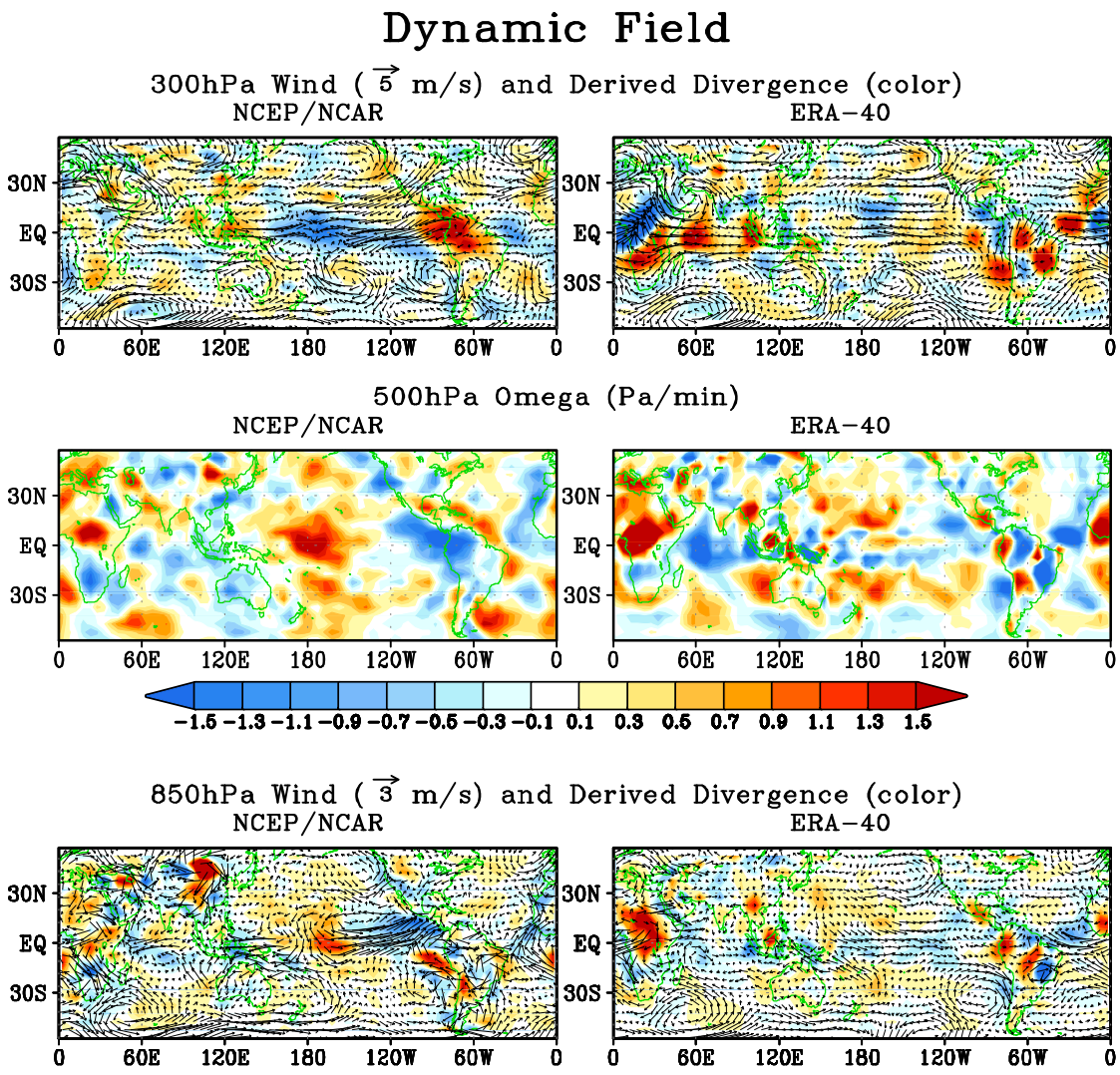

Figure 5. The representative spatial patterns of the dynamic variation associated with GW trend mode. Left column: from NCEP1-40p analysis, based on NCEP/NCAR reanalysis data. Right column: from ERE40-40p analysis, based on ERA-40 reanalysis data. Top row: the 300hPa horizontal wind field (vectors) and divergence derived from wind field (color, red represents positive value, blue represents negative value); middle row: the 500hPa vertical velocity field, positive value means descending motion; bottom row: similar as top row, but for 850hPa.

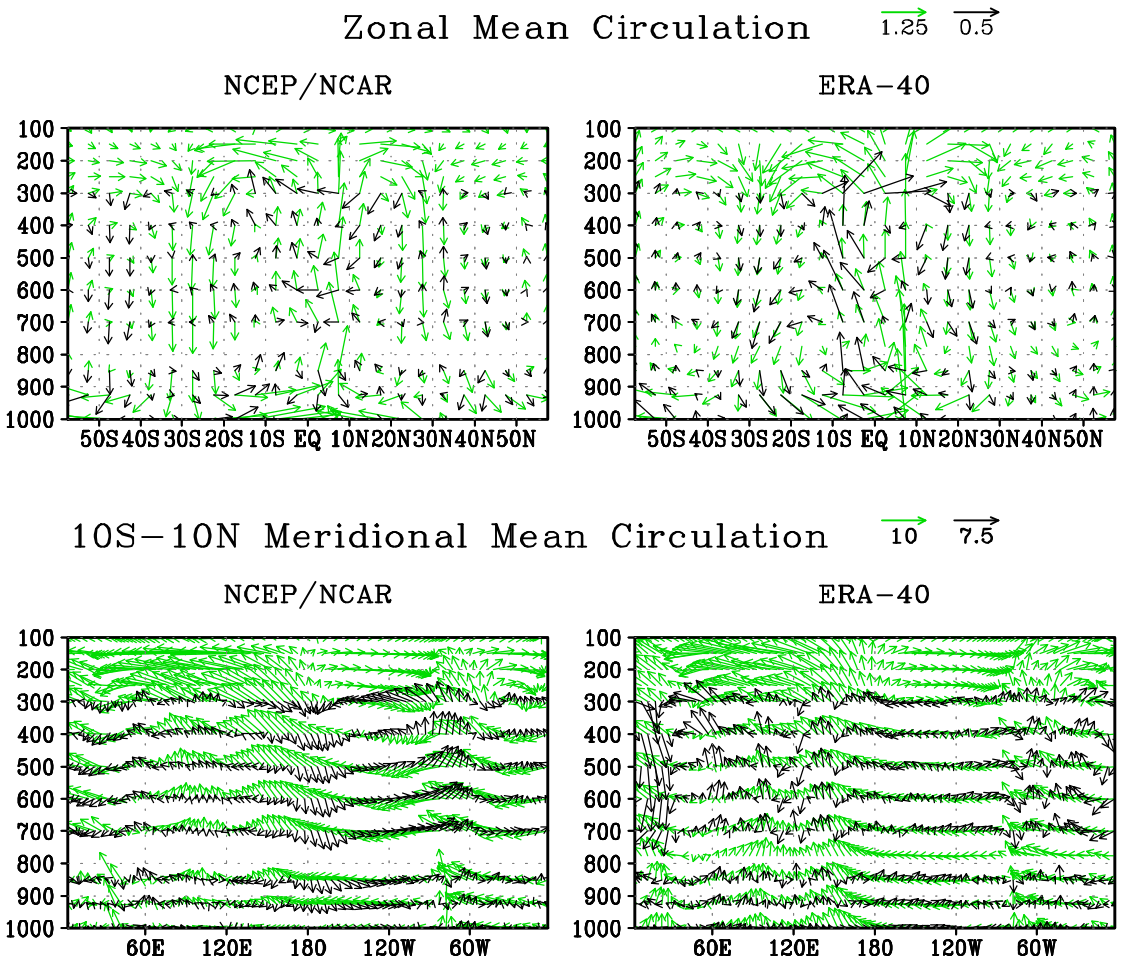

Figure 6. The circulation changes (black vectors) associated with the GW trend mode in the zonal mean meridional-vertical cross section (upper row) and the 10S-10N meridional mean zonal-vertical cross section (lower row). Left column: from NCEP1-40p analysis, based on NCEP/NCAR reanalysis data. Right column: from ERE40-40p analysis, based on ERA-40 reanalysis data. The climatology is drawn in green vectors. In the upper plots, the horizontal component of the vectors is meridional wind with unit 1(m/s), and the vertical component of the vectors is negative ω with unit –1/60(hPa/s). In the lower plots, the horizontal component of the vectors is zonal wind with unit 1(m/s), and the vertical component of the vectors is negative ω with unit –1/120(hPa/s). The arrow lengths of the vectors are scaled as shown on the top of each row.

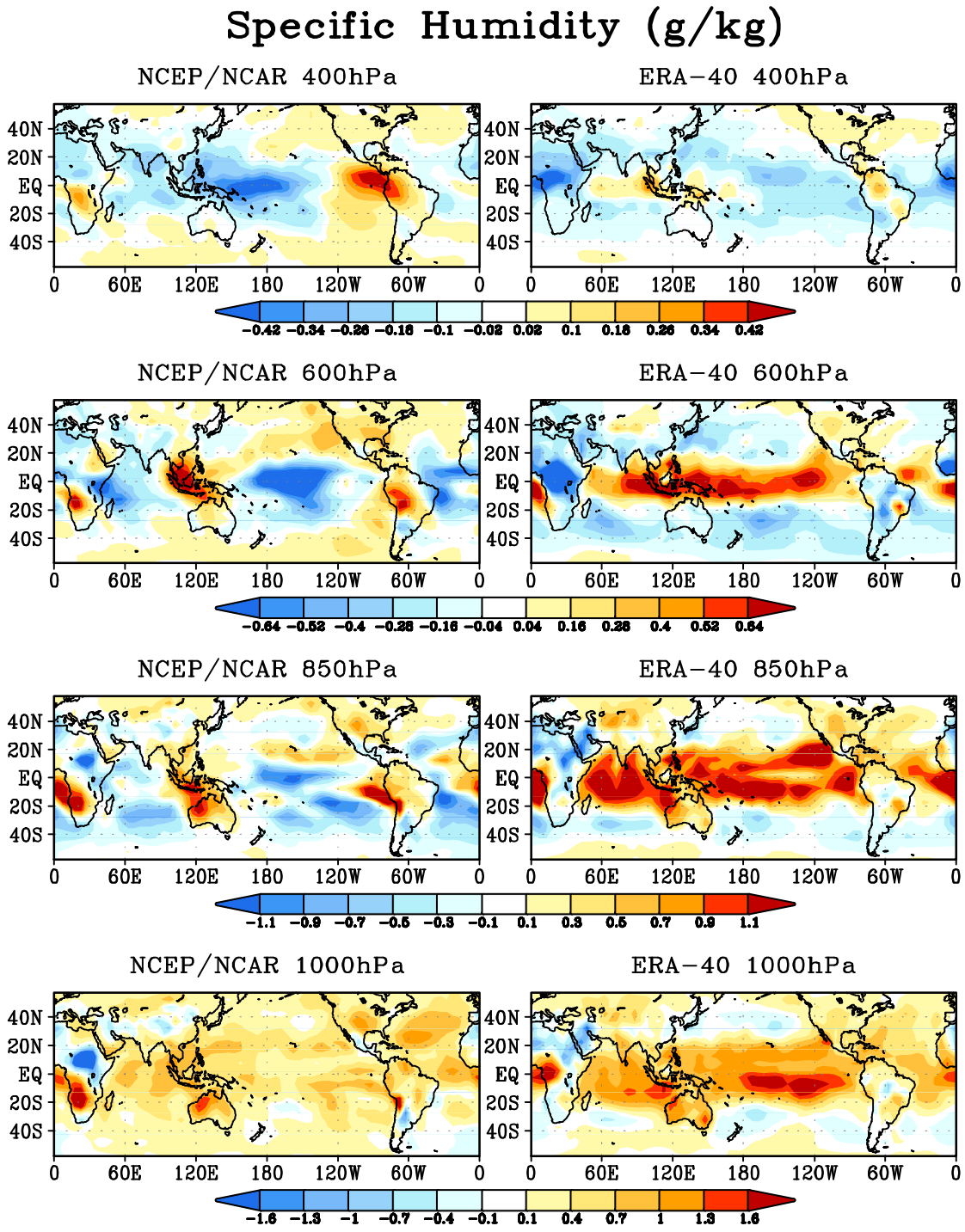

Figure 7. The q variation at selected pressure levels from 1000hPa to 300hPa associated with the GW trend mode. Left column: from NCEP1-40p analysis, based on NCEP/NCAR reanalysis data. Right column: from ERE40-40p analysis, based on ERA-40 reanalysis data.

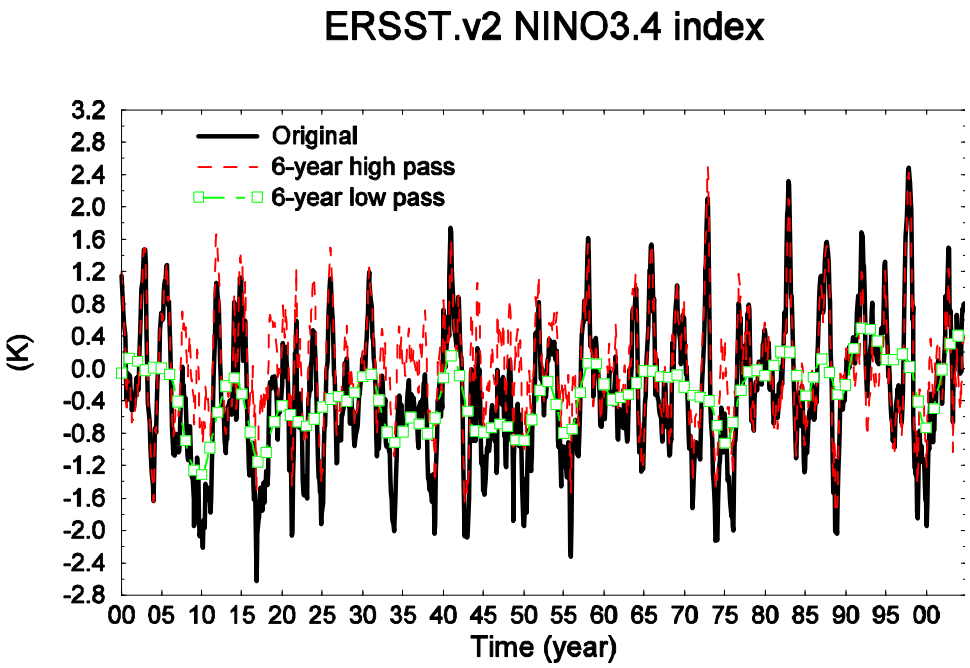

Figure A1. Black solid: The time series of the Niño-3.4 index, which is defined as the averaged SST anomaly in the equatorial Eastern Pacific region of 5˚N-5˚S and 170˚W-120˚W. It is calculated from ERSST.V2. Red dashed: 6-year high-pass filtered Niño-3.4 index (N34h), used the same filter as in Zhang et al. (1997). Green dot-dashed square: 6-year low-pass filtered Niño-3.4 index.

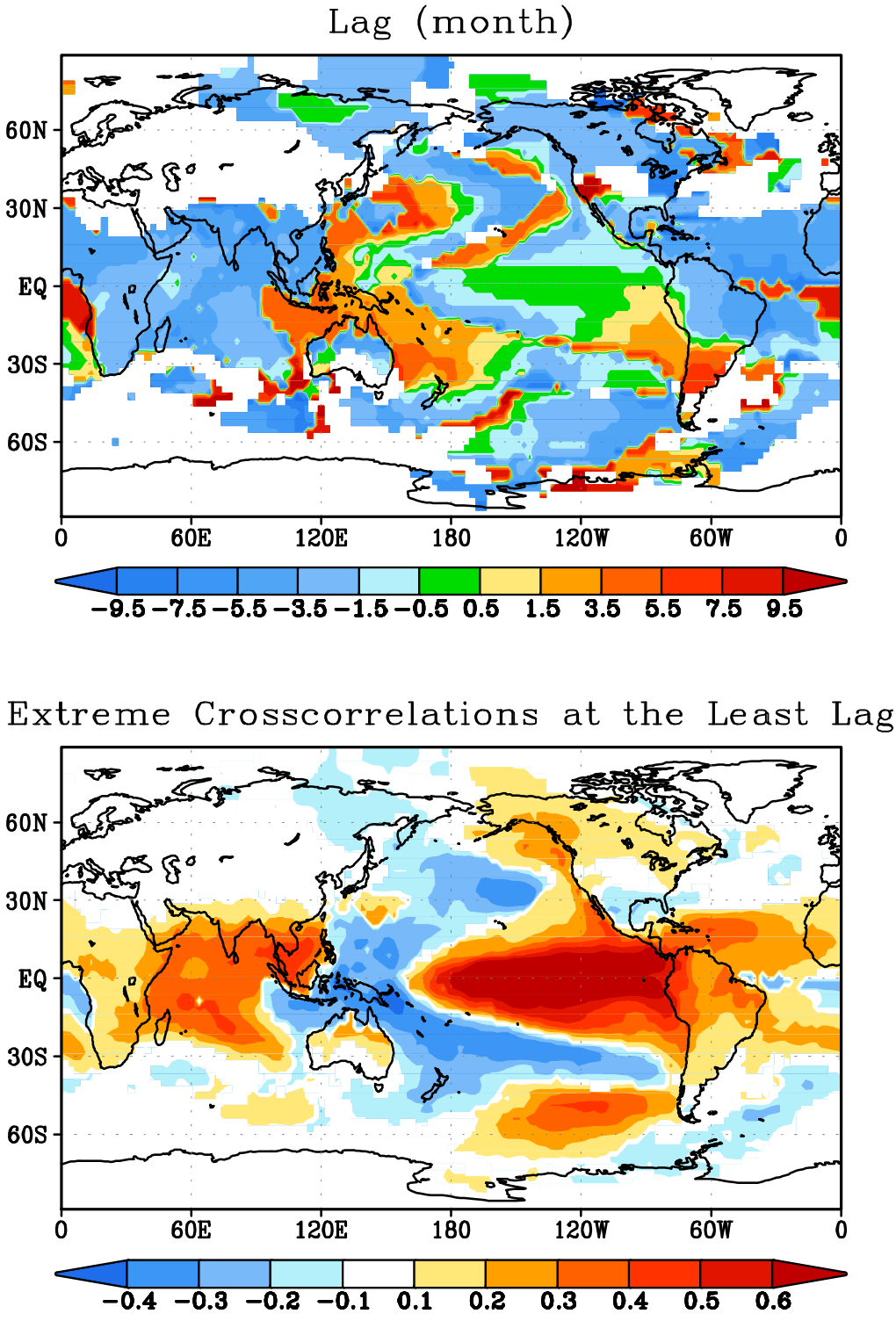

Figure A2. The map of extreme cross-correlations at the least lag (ECLL) of the N34h index with ST. Upper: the map of lags at which ECLL is found in ±12 month range. Negative value means the N34h index leads temperature. Lower: the values of ECLL. In these plots, only the values in the grids for which the ECLL confidence level exceeds 99% are shown.

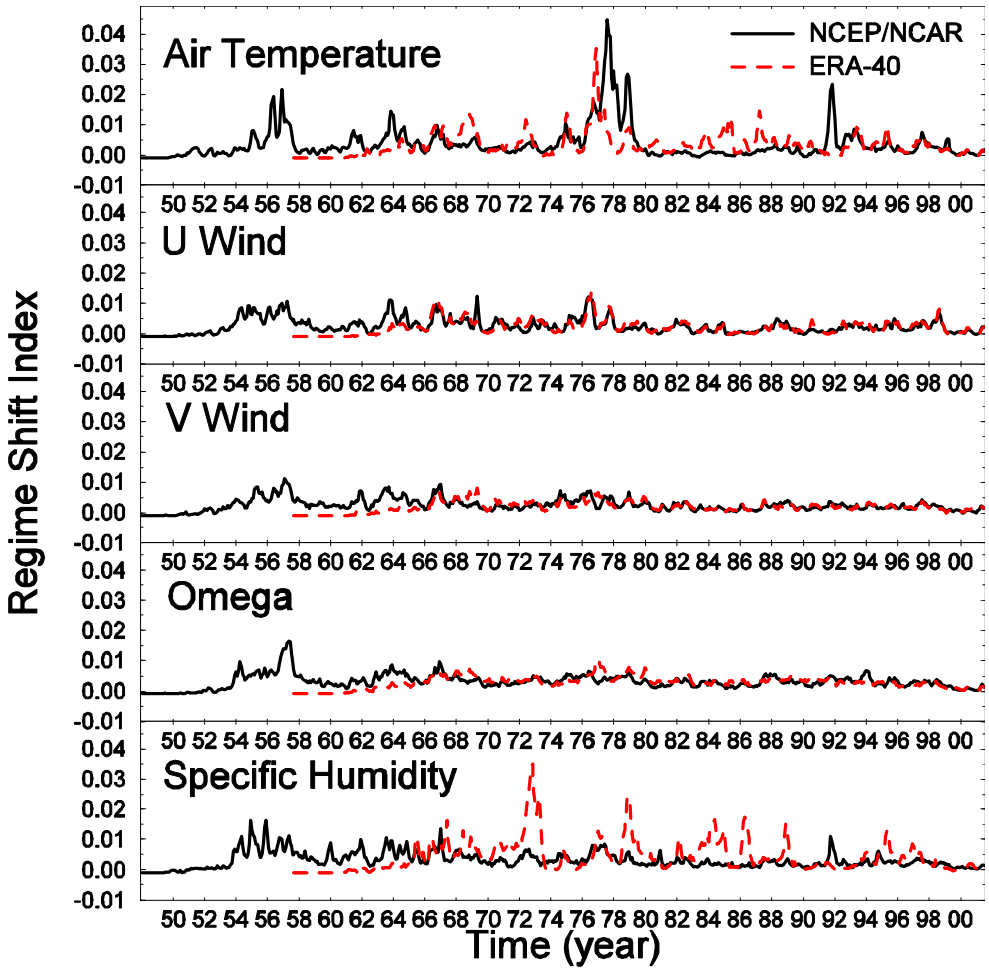

Figure B1. The global, 1000hPa-100hPa averaged discontinuity (RSI index defined in Rodionov, 2004) index time series for five atmospheric parameters (T_{air}, U, V, ω and q) from NCEP/NCAR (black solid) and ERA-40 (red dashed) reanalyses.

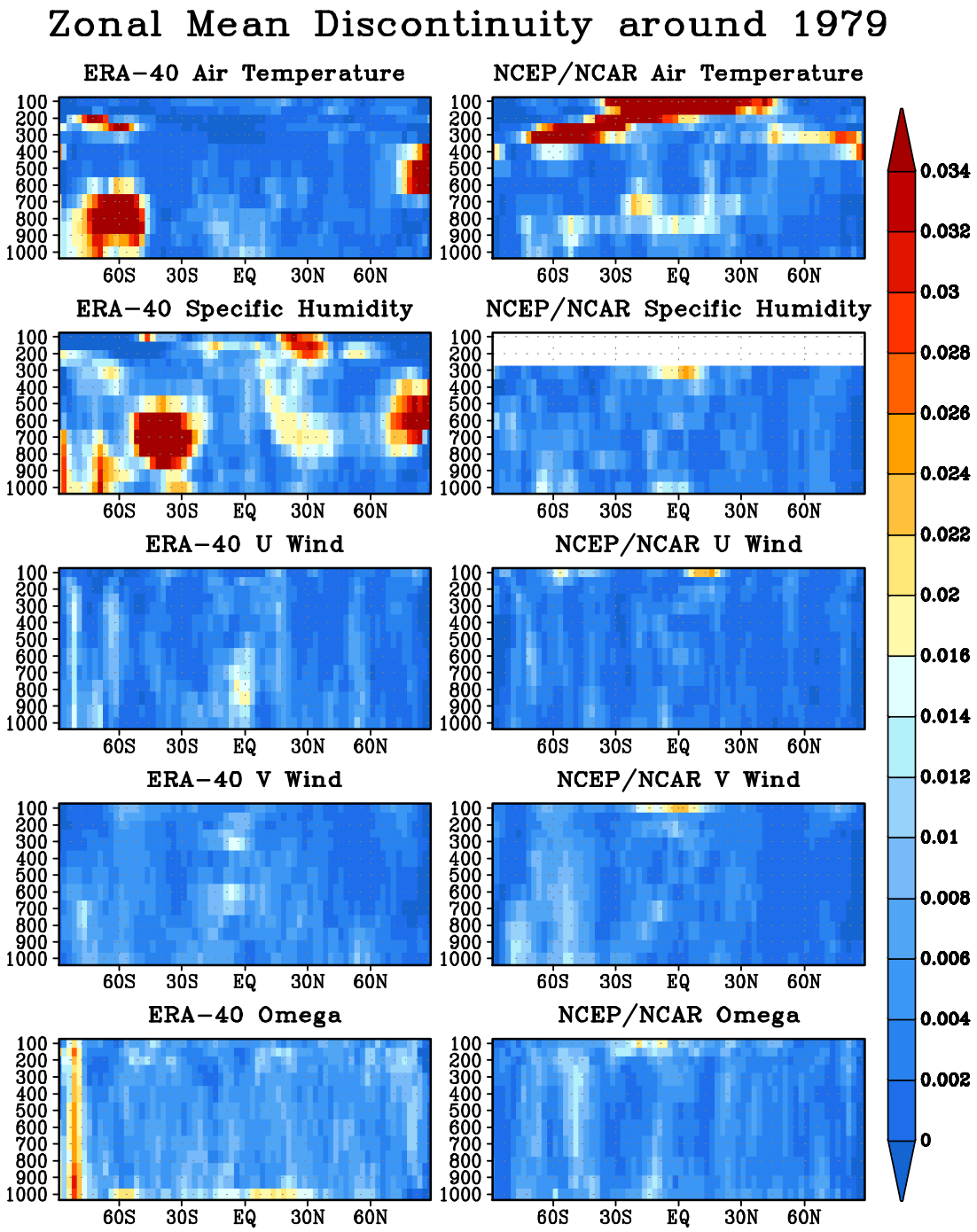

Figure B2. The zonal mean discontinuity index averaged around 1979 (from January 1978 to December 1979) for five parameters from NCEP/NCAR (right column) and ERA-40 (left column). The parameters shown from top to bottom: T_{air}, q, U, V, ω. The color bar shows the strength of the discontinuity; the horizontal axes are latitude, and the vertical axes are pressure level.

Table 1. The correlation coefficients between NCEP/NCAR reanalysis and ERA-40 reanalysis in GW spatial patterns.

	1000hPa	925hPa	850hPa	700hPa	600hPa	500hPa	400hPa	300hPa
T	0.65	0.49	0.11	0.27	0.50	0.61	0.68	0.52
U	0.59	0.63	0.53	0.39	0.48	0.47	0.46	0.53
V	0.43	0.42	0.45	0.52	0.56	0.58	0.59	0.60
ω	0.17	0.22	0.25	0.23	0.29	0.34	0.37	0.41
q	0.45	0.32	0.30	0.09	0.01	0.18	0.18	0.01